Fabrication of Multidimensional Surface-Enhanced Raman Spectroscopy (SERS) Substrates using Bioscaffolds

By: Gaius Hendrickson Justus St.Marie

A Thesis Submitted to

Saint Mary's University, Halifax, Nova Scotia

In Partial Fulfilment of the Requirements for the Degree of

Bachelor of Science with Honours in Chemistry

April 2019, Halifax, Nova Scotia

_____

Approved: Dr. Christa L. Brosseau

Supervisor

_____

Approved: Dr. Jason Masuda

Department Chair

Date: April 18, 2019

Certification

Fabrication of Multidimensional Surface-Enhanced Raman Spectroscopy Substrates (SERS) Substrates using Bioscaffolds

I hereby certify that this thesis was completed by Gaius Hendrickson Justus St.Marie in partial fulfillment of the requirements of the Degree of Bachelor of Science with Honours in Chemistry at Saint Mary's University and I certify that this is truly the original work carried out by Gaius Justus Hendrickson St.Marie.

Thesis Supervisor
Dr. Christa L. Brosseau

_____

Chairperson of the Chemistry Department
Dr. Jason Masuda

_____

Date: April 18, 2019

Abstract

Fabrication of Multidimensional Surface-Enhanced Raman Spectroscopy (SERS) Substrates using Bioscaffolds

By: Gaius Hendrickson Justus St.Marie

Plasmonics is the field of research which explores the unique optical and electronic effects observed when certain nanoscale metals interact with light. Plasmonic nanostructures that are uniform in size and shape are highly desirable for many applications, including plasmon-enhanced solar cells. Unfortunately, plasmonic structures are difficult and costly to prepare, which limits their widespread application in society. In this work, biological materials are used as scaffolds for the production of highly functional plasmonic materials. This thesis work explores five different biological materials: blue mussel shells, scarab beetle elytra, buttercup petals, damselfly wings and Japanese rice fish scales that are abundant in nature and exhibit interesting nanoscale order. Scanning Electron Microscopy (SEM) and Surface-Enhanced Raman Spectroscopy (SERS) were used to characterize each bioscaffold with a focus on developing an optimal substrate by varying the deposition parameters for physical vapour deposition (PVD). The results of this work demonstrate the significant enhancement of the SERS spectra in the case of both damselfly wings and buttercup petals and highlights the promise of using these bioscaffolds as affordable and sustainable SERS-active substrates.

April 18, 2019

Acknowledgements

I would like to thank my research supervisor, Dr. Christa Brosseau for her support and guidance during this research project. I would especially like to thank Dr. Christa Brosseau for allowing me to be a part of her research team over the last three years and Osai Clarke for his constant encouragement during my first summer. I would also like to thank the current and past Brosseau lab group members: Najwan Albarghouthi, Dalal Alhatab, Taylor Lynk, Kathleen Allen, Shruti Bindesri, Melanie Davidson, Reem Karaballi, Navya Kesevan, Kaleigh McLeod, Pema Sherpa, Ricardo Jebailey and Marwa Yasmin.

I would like to extend my gratitude to Alyssa Doué, Dr. Xiang Yang and Dr. Luke Murphy, as well as the chemistry department and chemistry society for their support. I would also like to thank the faculty in the chemistry department for providing me with a greater appreciation for this research field. Finally, I would like to express thanks to my family members: Boniface St. Marie, Catherine St. Marie, Shauna St. Marie, Peter St. Marie and Dhania St. Marie for guiding me throughout this project. In addition, I express thanks to God for giving me the strength to accomplish this research thesis.

Table of Contents Page

Abstract iii

Acknowledgements iv

List of Figures viii

List of Tables xiii

List of Abbreviations xiv

Chapter 1: Introduction 1

1.1 Research Goal 1

1.2 Literature Review 3

1.2.1 Plasmonics 3

1.2.2 Surface-Enhanced Raman Spectroscopy 6

1.3 Surface-Enhanced Raman Spectroscopy Substrates 8

1.3.1 Bioscaffold Substrates 8

1.3.2 Film-Over-Nanosphere Substrates 14

1.4 Theory 16

1.4.1 Raman Spectroscopy 16

1.4.2 Physical Vapour Deposition 18

Chapter 2: Experimental 21

2.1 Reagents and Materials 21

2.2 Microscopic Studies 21

2.3 Physical Vapour Deposition Parameters 22

2.4 Preparation of SERS Substrates using Bioscaffolds 22

2.4.1 Blue Mussel Shell 22

2.4.2 Scarab Beetle Elytra 23

2.4.3 Buttercup Petal 23

2.4.4 Damselfly Wing 23

2.4.5 Japanese Rice Fish Scales 24

2.4.6 Silver Film-Over-Nanospheres 24

Chapter 3: Results and Discussion 26

3.1 Scanning Electron Microscopy of Bioscaffolds 26

3.1.1 Blue Mussel Shell 26

3.1.2 Scarab Beetle Elytra 26

3.1.3 Buttercup Petal 27

3.1.4 Damselfly Wing 28

3.1.5 Japanese Rice Fish Scales 29

3.1.6 Silver Film-Over-Nanospheres 29

3.2 SERS of Bioscaffolds 31

3.2.1 Comparison of Silver Film-Over-Nanospheres and Silver Island-Films 31

3.2.2 Comparison of Bioscaffolds Based on SERS Signal 34

3.2.3 Effect of Silver Film Thickness on SERS Signal 40

3.3 Deposition Parameter Changes for Bioscaffolds 43

3.3.1 Parameter Change: Substrate Rotation 44

3.3.2 Parameter Change: Deposition Rate 48

3.3.3 Parameter Change: Current 50

Chapter 4: Conclusion 58

Chapter 5: Future Work 59

Chapter 6: References 60

Appendix 68

List of Figures

Figure	Figure Caption	Page #
1.2.1	The interaction between the oscillating electric field component of the incident light and the free electrons at the surface of the nanosphere.[4] Reproduced with permission.	**4**
1.2.2	Bar graph showing the number of publications within the term "Surface-enhanced Raman spectroscopy" in the title according to Web of Science v5.32, December 2018.	**6**
1.3.1	(a) Photograph of damselfly wing showing the blue-green iridescent colour present on the three-dimensional wing scale arrays. (b) Photograph of damselfly	**11**
1.3.2	(a) The buttercup petals are highly lustrous having a yellow gloss owing to a mirror-like reflection on the upper epidermis. (b) Photograph of buttercup flower.	**12**
1.3.3	(a) Photograph of beetle elytra. (b) Beetles are able to change the colour of its elytra from yellowish to black and back again to yellowish within a few minutes.[29]	**12**
1.3.4	Fish scales have a distinct silver colour and the scales contain microstructures with horizontal and vertical "struts".	**13**
1.3.5	(a) Photograph of a segment of the blue mussel shell. (b) Blue mussel shells are typically triangular-shaped and elongate with rounded edges.	**14**
1.3.6	Continuous island-film grown on glass substrates.	**15**
1.4.1	Diagram showing the different light scattering modes: Rayleigh, Stokes, and anti-Stokes scattering.	**17**
1.4.2	Schematic representation of the PVD process.[38]	**19**
3.1.1	(a) Photograph of blue mussel shell. (b) SEM image of blue mussel shell at 20.0 kV- 50x: 100 nm Ag deposition. (c) SEM image showing crevices present in the blue mussel shell taken at 20.0 kV- 40kx: 100 nm Ag deposition. (d) SEM image of blue mussel shell taken at 20.0 kV- 80kx: 100 nm Ag deposition.	**26**
3.1.2	(a) Photograph of beetle elytra. (b) SEM image of the beetle elytra at 20.0 kV- 50x: 100 nm Ag deposition. (c) SEM image of the beetle elytra taken at 20.0 kV- 40kx: 100 nm Ag deposition. (d) SEM image showing in-depth nanostructures present in the beetle elytra taken at 20.0 kV- 80kx: 100 nm Ag deposition.	**27**
3.1.3	(a) Photograph of buttercup petal. (b) SEM image showing the striations and pollen grains on the buttercup petal taken at 20.0 kV- 50x: 100 nm Ag deposition. (c) SEM image of the buttercup petal taken at 20.0 kV- 40kx: 100 nm Ag deposition (d) SEM image of the buttercup petal taken at 20.0 kV- 80kx: 100 nm Ag deposition.	**28**
3.1.4	(a) Photograph of damselfly wing. (b) SEM image showing the nanoridges present on the damselfly wing after a thin layer of silver deposited taken at 20.0 kV- 50x: 100 nm Ag deposition. (c) SEM image showing the ridges present in the damselfly wing taken at 20.0 kV- 40kx: 100 nm Ag deposition**.** (d) SEM image of the damselfly	**28**

wing taken at 20.0 kV- 80kx: 100 nm Ag deposition.

3.1.5	(a) Photograph of fresh water fish. (b) SEM image showing the circular-shaped fish scales after a thin layer of silver deposited taken at 20.0 kV- 50x: 100 nm Ag deposition. (c) SEM image showing the structure of a fish scale taken at 20.0 kV- 40kx: 100 nm Ag deposition. (d) SEM of the fish scale taken at 20.0 kV- 80kx: 100 nm Ag deposition.	**29**
3.1.6	(a) Photograph of the coverslip after drop-coating 5 µL of 680 nm polystyrene sphere solution and the surface after a thin film of silver (Ag) was deposited using PVD. (b) SEM image showing the bilayer of polystyrene sphere solution on the coverslip at 20.0 kV- 40 kx. (c) SEM image showing polystyrene nanospheres on the surface of the coverslip taken at 20.0 kV- 80 kx: 100 nm Ag deposition.	**31**
3.2.1	Average SERS spectra of p-ATP drop-coated on the silver film-over-nanospheres and silver island-film- 50nm Ag deposition using the 780 nm laser. (12.17 mW and acquisition time of 30 seconds)	**33**
3.2.2.1	SERS spectra of p-ATP on fish scale- 50nm Ag deposition using the 780 nm laser. (12.17 mW and acquisition time of 30 seconds)	**35**
3.2.2.2	EDX spectra of blue mussel shell- 50nm Ag deposition. (780 nm laser, 12.17 mW and acquisition time of 30 seconds)	**36**
3.2.2.3	SERS spectra of p-ATP on each bioscaffold- 50 nm Ag deposition. (780 nm laser, 12.17 mW and acquisition time of 30 seconds)	**36**
3.2.2.4	SERS spectra of p-ATP on each bioscaffold- 100 nm Ag deposition. (780 nm laser, 12.17 mW and acquisition time of 30 seconds)	**37**
3.2.2.5	SERS spectra of p-ATP on each bioscaffold- 150 nm Ag deposition. (780 nm laser, 12.17 mW and acquisition time of 30 seconds).	**38**
3.2.2.6	SERS spectra of p-ATP on each bioscaffold- 200 nm Ag deposition. (780 nm laser, 12.17 mW and acquisition time of 30 seconds).	**39**
3.2.3.1	(a) SERS intensity of p-ATP (1080 cm^{-1}) on beetle elytra at different thickness of Ag deposition. (b) SERS intensity of p-ATP (1080 cm^{-1}) on blue mussel shell at different thickness of Ag deposition. (780 nm laser, 12.17 mW and acquisition time of 30 seconds).	**41**
3.2.3.2	(a) SERS intensity of p-ATP (1080 cm^{-1}) on buttercup petal at different thickness of Ag deposition. (b) SERS intensity of p-ATP (1080 cm^{-1}) on damselfly wing at different thickness of Ag	**41**
3.3.1.1	deposition. (780 nm laser, SERS spectra of p-ATP on damselfly wing- 50 rpm. (780 nm laser, 12.17 mW and acquisition time of 30 seconds).	**44**
3.3.1.2	(a) SEM image showing surface of the damselfly wing- 50 rpm taken at 20.0 kV- 50x. . (b) SEM image showing the surface of the damselfly wing- 50 rpm taken at 20.0 kV- 40 kx: (c) SEM image showing the surface of the damselfly wing- 50 rpm taken at 20.0 kV- 80 kx: 150 nm Ag deposition.	**45**
3.3.1.3	SERS spectra of p-ATP on damselfly wing- 80rpm. (780 nm laser, 12.17 mW and acquisition time of 30 seconds).	**45**
3.3.1.4	(a) SEM image showing surface of the damselfly wing- 80 rpm taken at 20.0 kV- 50x. . (b) SEM image showing the surface of the	**46**

damselfly wing-80 rpm taken at 20.0 kV- 40 kx: (c) SEM image showing the surface of the damselfly wing-80 rpm taken at 20.0 kV- 80 kx: 150 nm Ag deposition. 780 nm laser. (12.17 mW and acquisition time of 30 seconds)

3.3.1.5 SERS spectra of p-ATP on buttercup petal- 50rpm. (780 nm laser, 12.17 mW and acquisition time of 30 seconds). **46**

3.3.1.6 (a) SEM image showing surface of the buttercup petal- 50 rpm taken at 20.0 kV- 50x. . (b) SEM image showing the surface of the buttercup petal- 50 rpm taken at 20.0 kV- 40 kx: (c) SEM image showing the surface of the buttercup petal- 50 rpm taken at 20.0 kV- 80 kx: 150 nm Ag deposition. **47**

3.3.1.7 SERS spectra of p-ATP on buttercup petal- 80rpm. (780 nm laser, 12.17 mW and acquisition time of 30 seconds). **47**

3.3.1.8 (a) SEM image showing surface of the buttercup petal- 80 rpm taken at 20.0 kV- 50x. . (b) SEM image showing the surface of the buttercup petal- 80 rpm taken at 20.0 kV- 40 kx: (c) SEM image showing the surface of the buttercup petal- 80 rpm taken at 20.0 kV- 80 kx: 150 nm Ag deposition. **48**

3.3.2.1 SERS spectra of p-ATP on buttercup petal- 1.00 Å/s. (780 nm laser, 12.17 mW and acquisition time of 30 seconds). **49**

3.3.2.2 (a) SEM image showing surface of the buttercup petal- 1.00 Å/s taken at 20.0 kV- 50x. . (b) SEM image showing the surface of the buttercup petal- 1.00 Å/s taken at 20.0 kV- 40 kx: (c) SEM image showing the surface of the buttercup petal- 1.00 Å/s taken at 20.0 kV- 80 kx: 150 nm Ag deposition. **49**

3.3.2.3 SERS spectra of p-ATP on damselfly wing- 4.00 Å/s deposition using the 780 nm laser. (12.17 mW and acquisition time of 30 seconds).
of p-ATP on beetle elytra at different thickness of Ag deposition using the 780 nm laser. (12.17 mW and acquisition time of 30 seconds). **50**

3.3.2.4 (a) SEM image showing surface of the damselfly wing- 4.00 Å/s taken at 20.0 kV- 50x. . (b) SEM image showing the surface of the damselfly wing- 4.00 Å/s taken at 20.0 kV- 40 kx: (c) SEM image showing the surface of the damselfly wing- 4.00 Å/s taken at 20.0 kV- 80 kx: 150 nm Ag deposition. **50**

3.3.3.1 SERS spectra of p-ATP on damselfly wing- 2.5 A. (780 nm laser, 12.17 mW and acquisition time of 30 seconds) **51**

3.3.3.2 (a) SEM image showing surface of the damselfly wing- 2.5 A taken at 20.0 kV- 50x. . (b) SEM image showing the surface of the damselfly wing- 2.5 A taken at 20.0 kV- 40 kx: (c) SEM image showing the surface of the damselfly wing- 2.5 A taken at 20.0 kV- 80 kx: 150 nm Ag deposition. **51**

3.3.3.3 SERS spectra of p-ATP on damselfly wing- 10 A. (780 nm laser, 12.17 mW and acquisition time of 30 seconds) **52**

3.3.3.4 (a) SEM image showing surface of the damselfly wing- 10 A taken at 20.0 kV- 50x. . (b) SEM image showing the surface of the **52**

damselfly wing- 10 A taken at 20.0 kV- 40 kx: (c) SEM image showing the surface of the damselfly wing- 10 A taken at 20.0 kV- 80 kx: 150 nm Ag deposition.

3.3.3.5 SERS spectra of p-ATP on buttercup petal- 2.5 A. (780 nm laser, 12.17 mW and acquisition time of 30 seconds). **53**

3.3.3.6 (a) SEM image showing surface of the buttercup petal- 2.5 A taken at 20.0 kV- 50x. . (b) SEM image showing the surface of the buttercup petal- 2.5 A taken at 20.0 kV- 40 kx: (c) SEM image showing the surface of the buttercup petal- 2.5 A taken at 20.0 kV- 80 kx: 150 nm Ag deposition. **53**

3.3.3.7 SERS spectra of p-ATP on buttercup petal- 10 A. (780 nm laser, 12.17 mW and acquisition time of 30 seconds). **54**

3.3.3.8 (a) SEM image showing surface of the buttercup petal- 10 A taken at 20.0 kV- 50x. . (b) SEM image showing the surface of the buttercup petal- 10 A taken at 20.0 kV- 40 kx: (c) SEM image showing the surface of the buttercup petal- 10 A taken at 20.0 kV- 80 kx: 150 nm Ag deposition. **54**

3.3.3.9 SERS spectra of p-ATP on buttercup petal, damselfly wing and AgFON. (780 nm laser, 12.17 mW and acquisition time of 30 seconds) **57**

A1 Average SERS spectra of p-ATP drop-coated on beetle elytra- 50 nm Ag deposition. (780 nm laser, 12.17 mW and acquisition time of 30 seconds) **68**

A2 Average SERS spectra of p-ATP drop-coated on beetle elytra- 100 nm Ag deposition. (780 nm laser, 12.17 mW and acquisition time of 30 seconds) **68**

A3 Average SERS spectra of p-ATP drop-coated on beetle elytra- 150 nm Ag deposition. (780 nm laser, 12.17 mW and acquisition time of 30 seconds) **69**

A4 Average SERS spectra of p-ATP drop-coated on beetle elytra- 200 nm Ag deposition. (780 nm laser, 12.17 mW and acquisition time of 30 seconds) **69**

A5 Average SERS spectra of p-ATP drop-coated on buttercup petal- 50 nm Ag deposition. (780 nm laser, 12.17 mW and acquisition time of 30 seconds) **70**

A6 Average SERS spectra of p-ATP drop-coated on buttercup petal- 150 nm Ag deposition. (780 nm laser, 12.17 mW and acquisition time of 30 seconds) **70**

A7 Average SERS spectra of p-ATP drop-coated on buttercup petal- 150 nm Ag deposition. (780 nm laser, 12.17 mW and acquisition time of 30 seconds) **71**

A8 Average SERS spectra of p-ATP drop-coated on buttercup petal- 200 nm Ag deposition. (780 nm laser, 12.17 mW and acquisition time of 30 seconds) **71**

A9 Average SERS spectra of p-ATP drop-coated on damselfly wing- 50 nm Ag deposition. (780 nm laser, 12.17 mW and acquisition time of 30 seconds) **72**

A10	Average SERS spectra of p-ATP drop-coated on damselfly wing- 100 nm Ag deposition. (780 nm laser, 12.17 mW and acquisition time of 30 seconds)	**72**
A11	Average SERS spectra of p-ATP drop-coated on damselfly wing- 150 nm Ag deposition. (780 nm laser, 12.17 mW and acquisition time of 30 seconds)	**73**
A12	Average SERS spectra of p-ATP drop-coated on damselfly wing- 200 nm Ag deposition. (780 nm laser, 12.17 mW and acquisition time of 30 seconds)	**73**
A13	Average SERS spectra of p-ATP on damselfly wing- 50 rpm (780 nm laser, 12.17 mW and acquisition time of 30 seconds)	**74**
A14	Average SERS spectra of p-ATP on damselfly wing- 80 rpm (780 nm laser, 12.17 mW and acquisition time of 30 seconds).	**74**
A15	Average SERS spectra of p-ATP on buttercup petal- 80 rpm (780 nm laser, 12.17 mW and acquisition time of 30 seconds).	**75**
A16	Average SERS spectra of p-ATP on buttercup petal- 1.00 Å/s (780 nm laser, 12.17 mW and acquisition time of 30 seconds).	**75**
A17	Average SERS spectra of p-ATP on damselfly wing- 4.00 Å/s (780 nm laser, 12.17 mW and acquisition time of 30 seconds).	**76**
A18	Average SERS spectra of p-ATP on damselfly wing- 2.5 A (780 nm laser, 12.17 mW and acquisition time of 30 seconds).	**76**
A19	Average SERS spectra of p-ATP on buttercup petal- 2.5 A (780 nm laser, 12.17 mW and acquisition time of 30 seconds).	**77**
A20	Average SERS spectra of p-ATP on buttercup petal- 10 A (780 nm laser, 12.17 mW and acquisition time of 30 seconds).	**77**

List of Tables

Table	Table Caption	Page #
3.2.3	Coefficient of variation for each bioscaffold calculated using 1080 cm^{-1} peak for p-ATP. The deposition thickness was varied using physical vapour deposition.	**42**
3.3.1	Coefficient of variation for ideal bioscaffolds using 1080 cm^{-1} peak. The parameters varied on the PVD included the deposition rate, rotation speed and current.	**55**

List of Abbreviations

SERS	surface-enhanced Raman spectroscopy
PVD	physical vapour deposition
SPR	surface plasmon resonance
EM	electromagnetic
3D	three-dimensional
p-ATP	para-aminothiophenol
AgNP	silver nanoparticles
AgFON	silver film-over-nanospheres
AgIF	silver island film
IR	infrared
PS	polystyrene
AFM	atomic force microscopy
SEM	scanning electron microscopy
CV	coefficient of variation

Chapter 1: Introduction

1.1 Research Goal

In the early 1970's it was observed by Fleischmann and colleagues that there was a large increase in the Raman signal for pyridine adsorbed onto the surface of an electrochemically roughened silver electrode.[1] While Fleishmann originally attributed the increased signal intensity to simple surface area increase, Van Duyne and Jeanmaire[2] and Albrecht and Creighton[3] independently reported in 1978 that that the source of the enhancement was also due to an enhanced electromagnetic field on the surface of the nanoscale metal features. In the ensuing years, the discovery of Surface-enhanced Raman spectroscopy (SERS) opened up a promising way to overcome the low-sensitivity problem associated with conventional Raman spectroscopy. The introduction of the SERS technique not only improved the overall surface sensitivity making Raman spectroscopy more applicable but also stimulated the study of the intricate relationship between the surface structure and optical characteristics that determined the signal intensity.[4]

Surface-enhanced Raman spectroscopy is also a powerful vibrational spectroscopy technique that allows for detection and identification of low concentration analytes through the Raman signal amplification afforded by enhanced local electromagnetic fields. SERS has progressed from simple studies of model systems on roughened electrodes to highly sophisticated studies such as single molecule spectroscopy on highly ordered substrates. It is now generally agreed upon that the dominant contributor to most of the SERS enhancement is the electromagnetic enhancement mechanism.[4] The electromagnetic enhancement mechanism is influenced by the interparticle spacing, the size and shape of the nanoparticle assemblies which generate numerous "hot spots". The

electromagnetic fields are strengthened by decreasing the interparticle spacing of coupled nanoparticle assemblies and are magnified exponentially among interparticle gaps and hot spots.[5]

To date, periodic ordered nanostructure arrays of noble metals with controllable size, shape and spacing on various substrates have been investigated as promising SERS substrates.[6] Current widely used SERS-active substrates include metal colloids, electrochemically roughened metal surfaces and vapour deposited metallic films. Based on the structure of the supporting substrate, electromagnetic enhancement for SERS is theoretically calculated to reach factors of $10^{10} – 10^{11}$.[5] However, limitations of the SERS technique include the fact that substrates can degrade over time resulting in a decrease in electromagnetic enhancement, there is generally poor reproducibility of the SERS signal within and among these substrates and there is a need for reusable, scalable and cost-effective SERS-active substrates.[6]

Recently, biomimetic synthesis has been developed as an alternative and interesting manufacturing method for the preparation of SERS-active substrates. Biomimetic synthesis refers to the use of biological materials (bioscaffolds) for the synthesis of SERS-active substrates. While most people perceive functional nanomaterials to be modern day constructs, nature is also full of such materials.[7] Naturally derived nanomaterials offer several advantages such as inherent stability, long-range order and biodegradability. Examples include the complex structures found in many insect wings, leaves and shells.[8] A key advantage of using natural biomaterials as scaffolds comes from their inherent complexity, a structural sophistication that has come about through millions of years of evolution.[8,9] Current research proves that biomimetic

SERS-active substrates have great practical potential applications in rapid, on-site trace detection of chemical, biological and hazardous materials.[8]

This project aims to explore the use of bioscaffolds in conjunction with physical vapour deposition for the fabrication of SERS-active substrates. The bioscaffolds that were studied include fish scales, buttercup petals, damselfly wings, beetle elytra and blue mussel shells. The main purpose was to fashion these bioscaffolds by physical vapour deposition by manipulating the different parameters such as deposition rate, film thickness and current. This deposition technique then produced a thin metal film onto each desired bioscaffold after which the Raman reporter *para*-aminothiophenol was drop-coated onto each bioscaffold to assess the SERS intensity.

1.2 Literature Review

1.2.1 Plasmonics

Plasmonics is the field of research which explores the unique optical and electronic effects observed when certain nanoscale metals interact with light. Plasmonic nanostructures require the presence of an oscillating electric field to generate plasmonic potential as a result of collective electron oscillation. In order to have sufficient plasmonic potential, Mie theory indicates that the metal under study should have a negative real and small imaginary component of its complex dielectric function.[10] For visible radiation, this requirement is best satisfied by silver (Ag), gold (Au) and copper (Cu). These plasmonic metals allow one to capture and manipulate light at the nanometer length scale in the visible wavelength region of the electromagnetic (EM) spectrum.

Plasmonic nanostructures that are uniform in size and shape are highly desirable for many SERS-based applications. The enhancement effects observed in SERS have been attributed to the electromagnetic (EM) mechanism possessed by plasmonic nanostructures which results from an increased local electromagnetic field (hot spot) at a metallic nanoparticle surface. Figure 1.2.1 shows the interaction of incident light and the free electrons of a metal nanosphere.

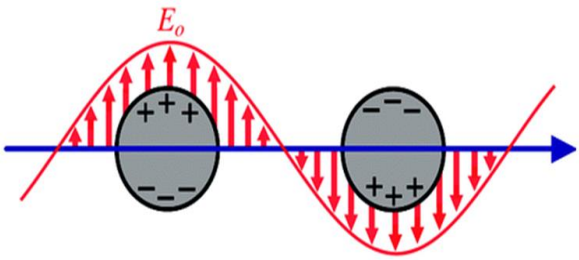

Figure 1.2.1: The interaction between the oscillating electric field component of the incident light and the free electrons at the surface of the nanosphere.[4] Reproduced with permission.

The EM mechanism, which is caused by the presence of plasmonic nanostructures on rough metal surfaces excited by the incident light contributes to the majority of the SERS enhancement.[11] The electromagnetic field enhancement is particularly strong at interparticle gaps and has led to the fabrication of SERS-active substrates with large SERS enhancement, high sensitivity, good reproducibility, uniformity and biocompatibility.[6]

Three-dimensional (3D) structures with nanogaps and nanobridges are considered to vastly improve the SERS enhancement compared to two-dimensional (2D) substrates

because of the simple fact that 3D structures supply more interparticle gaps and a larger surface area for adsorbing probe molecules than 2D substrates.[12] The 3D spatial structures supply more "hot spots" which provide a giant SERS enhancement because of the periodic sub-micrometer structures present in the surface. For example, in many butterflies, the wing scale has 3D periodic sub-micrometer structures which includes "main ridges", horizontal and vertical "struts" and "ribs" which clearly displays a 3D architecture feature.[13] These results indicate that the wing scales possess 3D morphologies that can be used as bioscaffolds for the preparation of 3D SERS-active substrates. Such structures, however, are quite difficult to prepare by traditional nanofabrication methods such as film-over-nanosphere lithography and electron beam lithography.

One promising route to create these 3D structures is direct replication from structures of various natural species.[6] Metals have been physically deposited onto biological structures to fabricate 3D structures through physical vapour deposition (PVD). This work will explore the use of bioscaffolds such as fish scales, damselfly wings, buttercup petals, beetle elytra and blue mussel shells that are low-cost, environmentally friendly and readily obtained. The potential application of these bioscaffolds is to produce a scalable SERS-active substrate with high sensitivity, good stability and ease of fabrication. This will be achieved by using physical vapour deposition to deposit a thin film of silver onto each bioscaffold under varying conditions after which the SERS performance will be assessed.

1.2.2 Surface Enhanced Raman Spectroscopy

Surface-enhanced Raman spectroscopy (SERS) has attracted increasing interest in several fields, such as materials science, environmental sciences, sensors, chemistry, biology, biophysics, and medicine. SERS is a variation of Raman spectroscopy in which the incoming laser beam interacts with electrons in plasmon oscillations in metallic nanostructures to enhance, by orders of magnitude, the vibrational spectra of molecules adsorbed to the nanostructure surface.[14] The size, shape and distribution of the metallic nanostructures is a primary factor determining the magnitude of signal enhancement and resulting detection sensitivity. SERS can be exploited as a label-free detection method able to provide ultra-high sensitivity within biomolecular and chemical sensing.[15] In 2016, over 800 papers were published on the topic; a decade earlier this number was less than 400. Results of a search of the Web of Science in the title index for the query "Surface-enhanced Raman spectroscopy substrates" supports this claim, as can be seen in Figure 1.2.2.

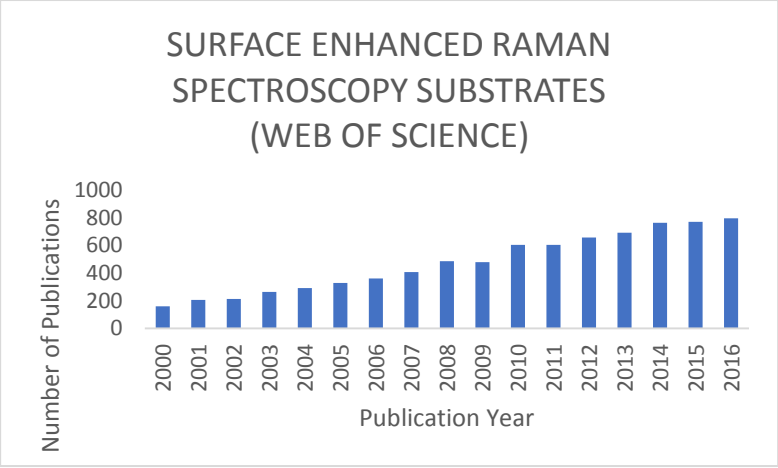

Figure 1.2.2: Bar graph showing the number of publications with the term "Surface-enhanced Raman spectroscopy substrates" in the title according to Web of Science v5.32, December 2018.

However, this remarkable analytical sensitivity has not translated into the development of practical in-situ SERS-active substrates. This is due in large part to the difficulty in easily preparing robust, metal-coated substrates of the correct surface morphology that provide maximum SERS enhancements. To date, most SERS-active substrates are composed of coinage metals (Au, Ag, Cu) in the form of roughened surfaces, nanoparticle aggregates or arrayed elements.[16] The use of bioscaffolds to produce SERS-active substrates offers a flexible, easy and inexpensive method for fabrication of integrated nanostructures for high sensitivity SERS applications. For highly optimized surfaces, SERS enhancement factors may approach $10^{10} - 10^{11}$; this strong electromagnetic field causes an increase in the induced dipole of the analyte molecule, resulting in more efficient, inelastic scattering.[17]

As a result of the sensitivity of SERS and the extreme localization of enhanced electric fields, much of the work with SERS is an attempt to create nanostructures with reproducible and controllable enhancements. Correlating the physical structure (the size, shape, morphology, and composition) with SERS enhancements has advanced both the understanding of SERS and the techniques used to control the assembly of nanostructures. The chemical enhancement in SERS is based on the polarizability changes of the adsorbed molecules on the metal surface, and the electron transfer between the adsorbate and the metal substrate. The electron transfer is facilitated by the excitation of electrons from the HOMO (highest occupied molecular orbital) to the LUMO (lowest unoccupied molecular orbital) in the molecule.[17]

More recent studies have attempted to probe the hot spot, which is the region with the highest electric field enhancement in single particles, in an attempt to determine the relative contribution of the hot spot to the SERS enhancement factor. SERS combined with plasmonic sensing can be used for high-sensitivity and quantitative detection of biomolecular interactions and to study redox processes.[18] This level of signal enhancement makes single molecule detection a possibility and the development of SERS-active substrates with high enhancement factors remains an active area of SERS research. SERS research is beneficial for environmental analysis, pharmaceuticals, art and archeological research, forensic science, drug and explosives detection, and food quality analysis.[19]

1.3 Surface-Enhanced Raman Spectroscopy Substrates

1.3.1 Bioscaffold Substrates

Bioscaffolds consisting of naturally ordered periodic nanostructures are currently being investigated as promising SERS-active substrates because of their excellent structural reproducibility and pronounced signal enhancement.[12] Flexible bioscaffolds have been developed as an alternative and interesting manufacturing method to the preparation of SERS substrates. Flexible bioscaffolds also have potential applications in low-cost embedded and integrated sensors for medical, environmental and industrial markets.[19]

Biological materials include ecofriendly substrates such as rose petals for ultrasensitive surface-enhanced Raman scattering (SERS).[20] The hydrophobic

concentrating effect of rose petals allows metal nanoparticle aggregates to bind on the surface.[21] The metal nanoparticles and analytes are both closely packed in the 3D structure of the lower epidermis. The nanogaps between adjacent silver nanoparticles dramatically enhanced the electric field and the Raman signals; however, the 3D distribution of nanoparticle aggregates on the lower epidermis contributed most efficiently to the SERS signals. The large area, dense nanoparticle aggregates on the rose petal provided a facile platform for the detection of trace amounts of rhodamine 6G.[20]

Likewise, butterflies belong to the order Lepidoptera that comprises an estimated 174 250 species.[13] A given species usually has more than one type of wing scale and as a result the morphological diversity offers a vast structure pool for biotemplating selection. In addition, chitin is the main component of butterfly wing scales and one of the richest natural polymer compounds.[22] The *Danaus genutia* butterfly wing was used as the template for the fabrication of 3D plasmonic structures.

The wing surface is covered with regularly arranged scales similar to Christmas tree-like structures. In the fabrication of the 3D Au nanostructures through physical vapour deposition, the butterfly wing was placed directly under an Au source so that Au atoms were deposited vertically on the wing structures.[23] After deposition, periodic strips of Au were observed on the surface. To reduce the optical contribution from the butterfly wing template, the 3D biotemplated Au nanostructures were immersed in a refractive index matching fluid. To confirm the near-field coupling effects, methylene blue was adsorbed onto the 3D plasmonic structures. As the thickness of the Au nanostrips increased, there was an increase in the SERS intensity, which can be attributed to the larger scattering efficiency.[24]

The hydrophobic and nano-hierarchical structures of mussel shell make it a durable, sensitive and reproducible SERS substrate. As a result of the hydrophobic concentration effect, silver and gold nanoparticles aggregate on the mussel shell.[21] The nano-hierarchical structures act as 3D templates for the assembly of nanoparticles. The periodic gratings on the mussel shell also made the distribution of nanoparticles with high periodicity on the SERS substrate a good candidate for the detection for Rhodamine 6G. The limit of detection for Rhodamine 6G was as low as 10^{-9} M and signal reproducibility could be significantly improved and measured with a variation of 6.5% for the peak at 613 cm^{-1}.[21] More importantly, the as-prepared substrate can be utilized for the fast discrimination of *Escherichia coli*, *Staphylococcus aureus* and *Pseudomonas aeruginosa* by discriminant analysis. Moreover, viruses offer a wide range of nanostructures, including a number of morphologies such as spheres, rods, and tubules that are monodisperse.

Upon the removal of the core genetic material, the resultant virus-like particle provides a hollow shell with the center of the nanostructure providing local field enhancements at the surface of the substrate.[25] The first metallic virus based bioscaffolds were produced using the *Chilo* iridescent virus as the dielectric core. Irregularities in the shell resulted in an increase in the effects of inhomogeneous broadening on the plasmon surface which led to the need for different fabrication routes for virus based bioscaffolds as a SERS-active substrate. Bioscaffolds offer several advantages such as inherent stability, long-range order and biodegradability.

A key advantage of using natural biomaterials as scaffolds comes from their inherent complexity and order. Light is scattered uniformly and completely in all

directions by utilizing the natural reflectors and photonic nanocrystals present in the wing scale and virus shell respectively. As a result, light is strongly reflected by constructive interference with the same phase fulfilling the condition for Bragg's Law.[26] Iridescence is caused by this interference pattern and is common in single layer reflectors found in nature whereby the effect varies with the angle of incidence. As the angle of incidence changes, the observed structural colour of the bioscaffold also changes. The beautiful iridescent colours of the damselfly wings (*Epiophlebia Laidlawi*) as depicted in Figure 1.3.1 are due not to pigments or colourants but instead to periodic physical structures; this is referred to as structural colour.[27]

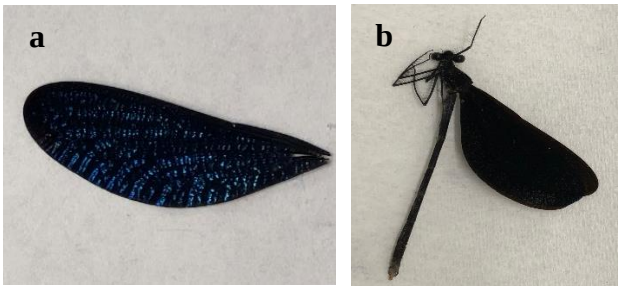

Figure 1.3.1: (a) Photograph of damselfly wing showing the blue-green iridescent colour present on the three-dimensional wing scale arrays. **(b)** Photograph of damselfly.

Buttercup petals (*Ranunculus repens*) are known for having a distinctive sheen. This special reflective quality is unique to the buttercup petal which is created by a special combination of pigments which create a thin film on the petal's outer layer. This flat, pigment-filled upper epidermis contains structures at the nanometer and the micrometer scale and are required to entrap air below water droplets thereby serving as a filter for light backscattered by the strongly scattering starch and mesophyll layers.[28] The petals consist of both micrometric protuberances and nanometric nubs and its durability to

different extreme conditions makes this a promising candidate for the practical application as a SERS-active substrate.[21]

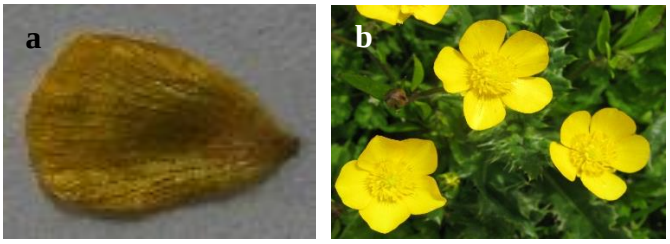

Figure 1.3.2: (a) The buttercup petals are highly lustrous having a yellow gloss owing to a mirror-like reflection on the upper epidermis. **(b)** Photograph of buttercup flower.

The range of optical reflectors and anti-reflectors in beetles is diverse, as a result of millions of years of evolution. Beetles (*Chrysophora chrysochlora*) possess scales on the outer elytra that are estimated to be 0.1 mm in diameter.[29] This is found in patches at the top and the side of the hemispherical body. The inner structure of the scales is a solid array of transparent spheres that are each 250 nm in diameter making the beetle elytra a potentially good SERS substrate. The spheres are arranged such that they have a precise and hexagonal-close-packing order to allow for reflection of a narrow range if wavelengths over a wide range of angles of iridescence.[27]

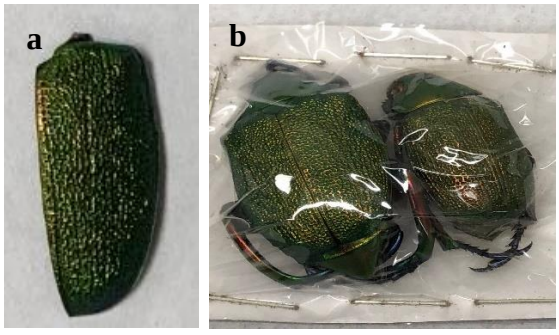

Figure 1.3.3: (a) Beetle elytra able to change the colour of its elytra from yellowish to black within a few minutes.[29]. **(b)** Photograph of Scarab beetle.

In fish scales (*Oryzias latipes*), the fish forces water through its gills that contains many tiny blood vessels causing the bright red colour. Photonic crystals are also present on the surface of these gills and are able to control the propagation of light.[27] Light interacts with the periodic surface of scales consisting of grooves in the structure that causes light to be scattered or diffracted from successive grooves causing the iridescent appearance present on fish scales.

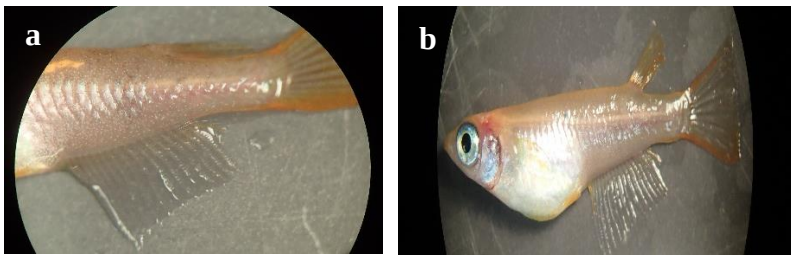

Figure 1.3.4: (a) Fish scales have a distinct silver colour and the scales contain microstructures with horizontal and vertical "struts". **(b)** Photograph of Japanese rice fish.

The blue mussel shell (*Mytilus edulis*) forms large scale three dimensional super crystals that show surface laminated structures and crossed nanoplates and nanochannels.[21] The shell is smooth with fine concentric growth lines but no radiating ribs. The shells of this species are purple, blue and brown in colour with radial stripes as shown in Figure 1.3.5 which is covered by a prismatic calcitic layer. More importantly, it was noted that the grating microstructures on the mussel shell gives the iridescent colour of the shell because of the interference and diffraction of natural light being distributed periodically.

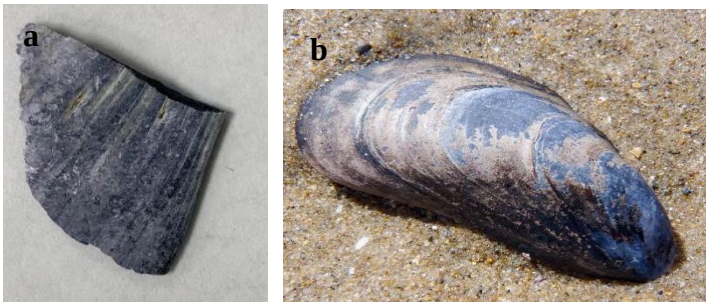

Figure 1.3.5: (a) Photograph of a segment of the blue mussel shell. **(b)** Blue mussel shells are typically triangular-shaped and elongate with rounded edges.

1.3.2 Film-Over-Nanosphere Substrates

Surface-enhanced Raman spectroscopy (SERS) is a widely used technique for obtaining vibrational spectra at some roughened metal surfaces.[1] Van Duyne and Creighton noted that Raman scattering is increased 3-6 orders of magnitude when a compound is adsorbed on a roughened silver surface.[1,3] However, the current lack of information concerning the detailed three-dimensional (3D) structure of SERS-active substrates is an obstacle to extending the scope of SERS. The formation of nanostructures to solve the poor reproducibility of the SERS-active sites remains a key challenge in this field. In light of this, a unique SERS platform consisting of a metal film over close-packed nanosphere substrate was first developed in 1984.[30]

Metal film-over-nanosphere (MFON) substrates are created by vapour deposition of thin films of either silver or gold over spheres (polystyrene or silica) and are optimal SERS substrates in that they are easily made and are cost effective. The main parameters that determine the practicability of these metal film-over-nanospheres are roughness and thickness of the film and the type of the metal used for deposition. In light of this, the use

of thin metal films has been considered as ideal substrates for exploring the relationship between surface coverage and SERS intensity.

Van Duyne proposed silver island films (AgIF) and silver film-over-nanospheres (AgFON) as SERS-active substrates in order to improve the surface stability of these glass substrates.[31] Silver-island films are SERS-active substrates that produces continuous island-like particles that are more stable than sols as depicted in Figure 1.3.6. As in the case of roughened electrodes and metal sols, the structures of the particles are dependent on several experimental factors, including the substrate material, the temperature of the substrate during and following metal deposition, the thickness of the film and the rate of metal deposition.[32] These conditions are easy to control and reproducible SERS-active island films can be prepared by physical vapour deposition.

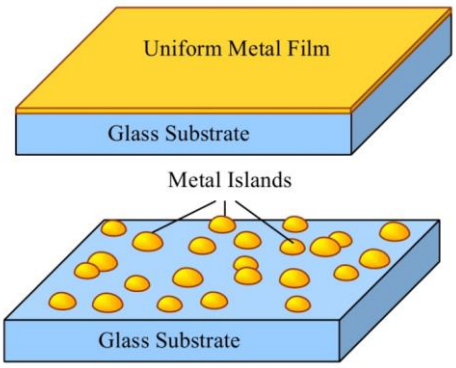

Figure 1.3.6: Continuous island-film grown on glass substrates.

The surface roughness and nanometer structure of the films are characterized using atomic force microscopy (AFM) and scanning electron microscopy (SEM) for thick evaporated silver island films and silver film-over-nanospheres (AgFON).[33] AgFON surfaces are distinguishable because of a monolayer of polymer nanospheres (AgFON) which adds random roughness to the surface structure of the glass substrate. AgFON

surfaces have been shown to enhance thin film-based surfaces with a colloidal suspension of polystyrene spheres.[33] The AgFON substrate can serve as a SERS-active substrate for SERS detection with high sensitivity, good reproducibility and high reliability because there are plenty of hot spots on its surface because of the unique structure of the polystyrene and silica spheres. It has been shown that the hot spots which contribute to the enhancement of the SERS signal are usually located at the gaps and the corners of the polystyrene spheres.[31]

1.4 Theory

1.4.1 Raman Spectroscopy

Raman spectroscopy is a popular spectroscopic technique that is based on the inelastic scattering of light. The scattering process happens between a photon and a molecule.[34] The molecule can relax to emit a photon with less energy than the incident photon; this is known as Stokes shifted Raman scattering. In Raman scattering, the applied field induces an oscillating dipole in the molecule on the surface. This dipole then radiates, and there is a small probability that the radiated light is Stokes shifted by the vibrational frequency of the molecule.[35] In addition, if the molecule is already in an excited state and is excited to a higher virtual state, and it then relaxes back down to the ground state, emitting a photon with more energy than the incident photon; this is known as anti-Stokes Raman scattering.[36]

The incident photon assumes a different frequency after the interaction; the frequency difference is characteristic of the molecular vibrations. The shift in frequency

of the scattered photons can be greater than (anti-Stokes shift) or less than (Stokes shift) the frequency of the incident photons, and the direction of the shift is governed by whether the illuminated species of interest is in a vibrational excited state or the ground state.[34] When a photon is excited from a state higher than the ground state and the frequency of relaxation is more than the frequency of the incident light, anti-Stokes lines appear on the Raman spectrum.[37] Figure 1.4.1 shows the Rayleigh, Stokes, and anti-Stokes scattering of light.

Stokes lines are more intense than anti-Stokes lines, as the intensity of Stokes lines is proportional to the number of molecules in the ground state and the intensity of anti-Stokes lines is proportional to the number of molecules in an excited state, which is less populated.[1,36] As a result of the increased intensity displayed by Stokes lines, it is typically chosen to be monitored in conventional Raman spectroscopy. By observing Stokes scattering, it is easier to obtain the vibrational spectrum of the sample being analyzed, which is complementary to the more common infrared spectroscopy.

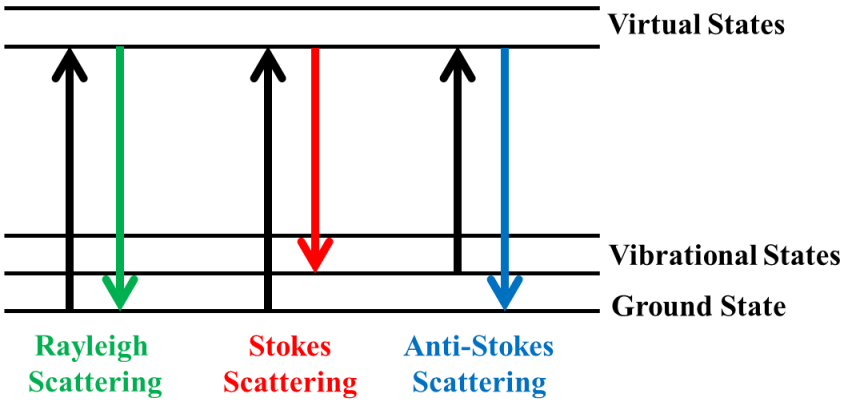

Figure 1.4.1: Diagram showing the different light scattering modes: Rayleigh, Stokes, and anti-Stokes scattering.

Unlike in infrared spectroscopy, where chromophores tend to have similar absorption strengths, polarizability is a significant factor that affects the intensity of the Raman signal since it depends on the ability of an electron cloud to interact with an electric field.[37] Polarizability measures the ease with which the electron cloud around a molecule can be distorted. Raman scattering occurs because a molecular vibration can change the polarizability making the electron clouds with delocalized electrons more susceptible to agitation by an incident electric field.

1.4.2 Physical Vapour Deposition

Physical vapour deposition (PVD) is a vacuum deposition method used to deposit thin films by the condensation of a highly purified metal onto a substrate. PVD is often done in a "good" vacuum environment.[38] The term "good" vacuum environment means that the deposition unit provides a long mean free path for collision between the vaporization source and the substrate further allowing the user to control the amount of gaseous and vapour contamination during processing. The "good" vacuum environment is generated by a vacuum system that includes the deposition chamber, substrate chambers ("substrate-lock chambers") if used, vacuum pumping systems at a typical pressure of 10^{-6} Pa, exhaust systems and a gas inlet system.[39]

The mere fact that physical vapour deposition is a coating process means that during deposition, the film can be contaminated by system-related contamination and by process-related contamination. Physical vapour deposition has a high process cost and it is considered less environmentally friendly than traditional coating processes such as electroplating and painting.[40] It is important to note that compared to current top-down

techniques such as electron beam lithography, physical vapour deposition is scalable, less expensive and PVD is capable of coating complex shapes. The fixturing and tooling used to hold, position and move the substrates are important to the PVD system design and ensures that the typical PVD process is carried out in "good" vacuum system. The most important steps involved in the PVD process are presented in Fig. 1.4.2.

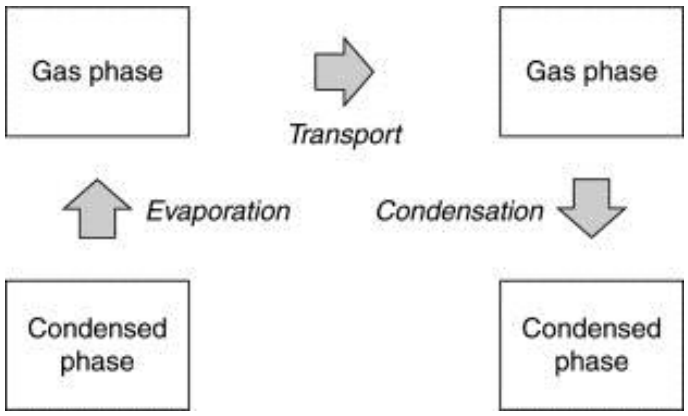

Figure 1.4.2: Schematic representation of the PVD process.[38]

In physical vapour deposition, a purified metal pellet goes from a condensed phase to a vapour phase and then back to a thin film condensed phase.[42] Many different types of SERS substrates have been described over the years; however, each type has its advantages and disadvantages that are tightly correlated with the method of fabrication. In general, physical vapour deposition coatings are more corrosion resistant than coatings applied by electroplating processes and electron beam evaporation. The thin film coatings have high temperature resistance and good impact strength, as well as excellent abrasion resistance.[40]

This thin metal film can be manipulated by adjusting the parameters on the physical vapour deposition system. Film thickness, deposition rate, power, substrate rotation and current are just a few of the parameters that can affect the layer of silver that is deposited on the substrate. The change in deposition rate and substrate rotation of vapour species causes microstructural changes which affects the adhesion strength and particle size of the metal film. Currently, metals are being physically deposited onto biological structures to fabricate metallic structures through physical vapour deposition by making use of the nanoscale cavities and indentations in the structures.[43]

2. Experimental

2.1 Reagents and Materials

Polystyrene microspheres (9.9% solids) with a mean diameter of 0.62 micrometres were purchased from Bangs Laboratories (Indiana, USA). Aluminium deposition targets (99.7% purity) and silver deposition targets (99.999% purity) were supplied by Angstrom Engineering (Kitchener Ontario, Canada). Damselflies (*Epiophlebia Laidlawi*) and scarab beetles (*Chrysophora chrysochlora*) were purchased from Thorne's Insect Shop Limited (London, Ontario, Canada). Blue mussel shells (*Mytilus edulis*) and buttercup petals (*Ranunculus repens*) were both obtained locally during the summer of 2018. Japanese rice fish (*Oryzias latipes*) were obtained from Aquatic Research Organisms, New Hampshire, USA. All solutions were prepared using Millipore water (≥18.2 MΩ cm). Glassware was cleaned in concentrated sulfuric acid and thoroughly rinsed with Millipore water prior to use.

2.2 Microscopic Studies

Substrates were imaged using a TESCAN MIRA 3 LMU Variable Pressure Schottky Field Emission Scanning Electron Microscope, this allowed for high magnification and resolution studies. (Pennsylvania, USA). This Field Emission Scanning Electron Microscope (FE-SEM) has a tungsten electron gun and is fitted with both a back scatter and a secondary electron detector. Energy dispersive X-ray spectra (EDS) were collected using an INCA X-max 80 mm^2 EDS system that uses a silicon drift detector (SDD). This was used to obtain qualitative information regarding the composition of the

SERS substrates. SEM image processing was done with the assistance of ImageJ software (NIH, Maryland, USA).

2.3 Physical Vapour Deposition Parameters

The physical vapour deposition unit supplied by Angstrom Engineering (COVAP), (Kitchener Ontario, Canada) allowed for the controlled deposition of silver onto the bioscaffolds. The metal deposition was monitored using a quartz crystal microbalance (QCM sensors, Lytron MCS Modular Cooling System). The system was set to a maximum power of 40.0% and pumped down to a pressure typically below 10^{-6} Pascal. The initial rate of deposition was set to 2.0 Å/s with the final thickness of silver deposited onto the substrate being adjusted from 0.500 kÅ (50 nm) to 2.000 kÅ (200 nm). The adjusted tooling factor for silver deposition was set to 27.0% to compensate for the difference between the film thickness measured using a profilometer on the substrate and the thickness reported by the QCM monitor.

2.4 Preparation of SERS Substrates using Biological Scaffolds

2.4.1 Blue Mussel Shell (*Mytilus edulis*)

The blue mussel shell has two different layers. The outer layer is typically composed of organic material such as biomineralized proteins, while the middle layer is composed of elongated crystals of calcium carbonate.[21] The sample was prepared for deposition by washing the substrate with ethanol (95%) and Millipore water. The substrate was left to dry overnight in a petri-dish and then attached to the substrate holder in the deposition unit via attachment clips.

2.4.2 Scarab Beetle Elytra (*Chrysophora chrysochlora*)

The beetle wings have evolved into hard covers called elytra. The elytra were removed using a scalpel. The exoskeleton of the beetle is made of hard plates of chitin.[43] The beetle elytra were rinsed with ethanol (95%) and Millipore water for five minutes respectively and then left to dry overnight. The elytra were placed on the substrate holder prior to silver deposition by PVD.

2.4.3 Buttercup Petal (*Ranunculus repens*)

Buttercup petals are lustrous, iridescent, and yellow in appearance as a result of the colouration mechanism. This is based on the petal's upper surface being very smooth causing a mirror-like reflection.[20] The epidermis is separated from the lower layers of the petal by an air gap. Reflection of light by the smooth surface of the cells and by the air layer effectively doubles the gloss of the petal.[27] The petals were rinsed with Millipore water for five minutes and left to air dry before being mounted onto a microscope slide which was attached to the deposition unit. The morphologies of the samples were observed using the SEM.

2.4.4 Damselfly Wing (*Epiophlebia Laidlawi*)

The damselflies were obtained from Thorne's Insect Shop. Each damselfly wing was removed using a scalpel and tweezers. The wings were then rinsed in ethanol (95%) and Millipore water for five minutes respectively and then naturally dried. The damselfly wings were fixed onto glass microscope slides before deposition and attached to the substrate holder using the attachment clips in the deposition unit.

2.4.5 Japanese Rice Fish Scales (*Oryzias latipes*)

The freshwater fish scale has a unique stacking structure which varies from opaque to translucent. The fish scale was removed using the scalpel and rinsed in Millipore water for five minutes and left to air dry before placement onto a microscope slide which was attached to the deposition unit.

2.4.6 Silver Film-Over Nanospheres (AgFON)

The glass substrates (microscope slides and 18 mm coverslips) were obtained from Fisher Scientific Ontario, Canada and were cleaned in piranha, which is a 3:1 v/v% sulfuric acid and 30% hydrogen peroxide. Glass substrates were pretreated in two steps: (1) piranha etch (caution: piranha solution should be handled with great care), 3:1 H_2SO_4:30% H_2O_2 at 80 ^oC for 1 h, was used to clean the substrate and (2) base treatment, 5:1:1 H_2O:NH_4OH:30% H_2O_2 with sonication for 1 h, was used to render the surface hydrophilic.[31] The substrates were then rinsed with Millipore water and sonicated for an hour in water.[44]

The microscope slides and coverslip substrates were then stored, and 5 µL of polystyrene sphere solution was drop coated onto the coverslip. By holding the coverslip with the tweezers, the drop of polystyrene sphere solution was poured over the entire surface of the coverslip by gently rotating the slide.[45] The prepared coverslips were put on a flat surface and left to dry naturally. Many research groups have used Triton X-100 in addition to the polystyrene sphere solution because it was proved to increase the monolayer area of deposited polystyrene. Triton X-100 reduces the surface tension and increases the hydrophilicity of the surface of the polystyrene spheres making it easier for

the particles to settle one next to the other.[31] The substrates were modified by the deposition of silver from 0.500 kÅ (50 nm) to 2.000 kÅ (200 nm) onto the polystyrene microspheres and the morphology was analyzed using the SEM.

Chapter 3: Results and Discussion

3.1 SEM of Bioscaffolds

3.1.1 Blue Mussel Shell

The following figures show photographs and electron micrographs for each bioscaffold investigated in this thesis. The three-dimensional structures present on the surface of the blue mussel shells were characterized using the SEM (Figure 3.1.1). The figures show high and low-magnification images of the striations present on the blue mussel shell. It must be noted that the blue mussel shell showed high mechanical and tensile strength as compared to other bioscaffolds under study such as the damselfly wings, buttercup petals, fish scales and beetle elytra. There was a clear distribution of regular arrays across the surface of the blue mussel shell as depicted in Figure 3.1.1a.

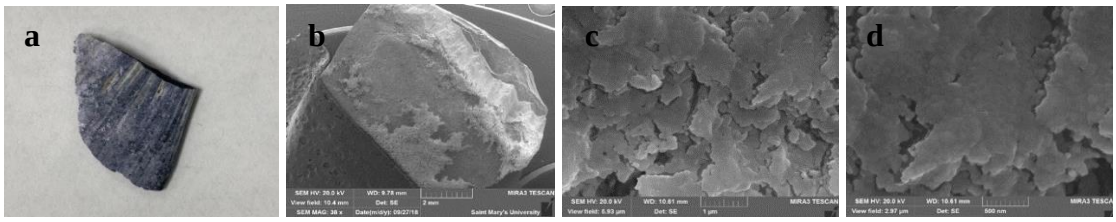

Figure 3.1.1 (a) Photograph of blue mussel shell. **(b)** SEM image of blue mussel shell at 20.0 kV- 50x: 100 nm Ag deposition. **(c)** SEM image showing crevices present in the blue mussel shell taken at 20.0 kV- 40kx: 100 nm Ag deposition **(d)** SEM image of blue mussel shell taken at 20.0 kV- 80kx: 100 nm Ag deposition.

3.1.2 Scarab Beetle Elytra

The scarab beetle elytra contain spatial structures (Figure 3.1.2). These spatial structures promote iridescence on the outer wing indicated by the greenish-yellow appearance.[29] The spatial structures contained many tiny scales embedded in the elytra as

noted in the SEM image at 80kx as shown in Figure 3.1.2d. The SEM images showed periodic sub-micrometer structures on the wing scale indicating that the beetle elytra possessed an intricate three-dimensional array structure.

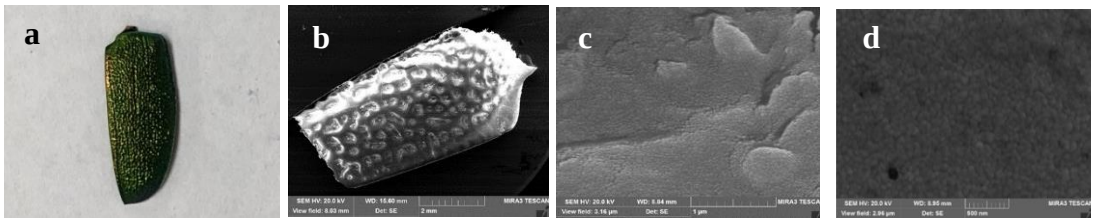

Figure 3.1.2 (a) Photograph of beetle elytra. **(b)** SEM image of the beetle elytra at 20.0 kV- 50x: 100 nm Ag deposition. **(c)** SEM image of the beetle elytra taken at 20.0 kV- 40kx: 100 nm Ag deposition. **(d)** SEM image showing the in-depth nanostructures present in the beetle elytra taken at 20.0 kV- 80kx: 100 nm Ag deposition.

3.1.3 Buttercup Petal

The buttercup petals were noted as having vertical ridges along their outer surface (Figure 3.1.3). These vertical ridges indicate that the petal was net-veined and at an in-depth view pollen grains were also present on the surface at 50x using the SEM as depicted in Figure 3.1.3b. The surface information observed using the SEM showed regular and even cross-distributed striations across the petal, the diameter of these striations increased gradually to the tip of the buttercup petal and was narrower at the base of the petal.

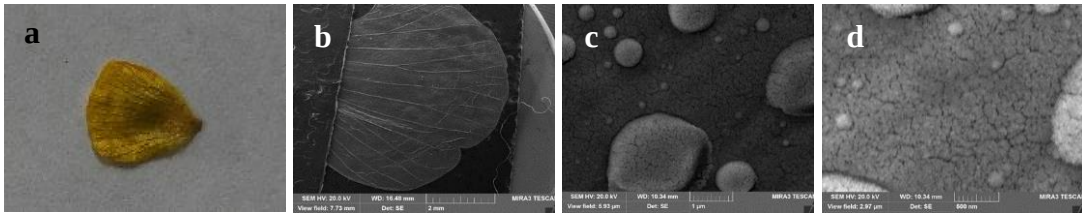

Figure 3.1.3 (a) Photograph of buttercup petal. **(b)** SEM image showing the striations and pollen grains on the buttercup petal taken at 20.0 kV- 50x: 100 nm Ag deposition. **(c)** SEM image of the buttercup petal taken at 20.0 kV- 40kx: 100 nm Ag deposition **(d)** SEM image of the buttercup petal taken at 20.0 kV- 80kx: 100 nm Ag deposition.

3.1.4 Damselfly Wing

The damselfly wings showed horizontal protrusions with a high degree of regularity in each Scanning Electron Microscopy (SEM) image (Figure 3.1.4). The damselfly wing substrates were fixed on the glass slides without damaging the damselfly wing as much as possible and the wing was coated with silver. The damselfly wings are mainly composed of veins and membranes, a typical nanocomposite material as shown in Figure 3.1.4b. The veins and membranes have a complex design within the wing that results in the damselfly being versatile and maneuverable fliers.[46]

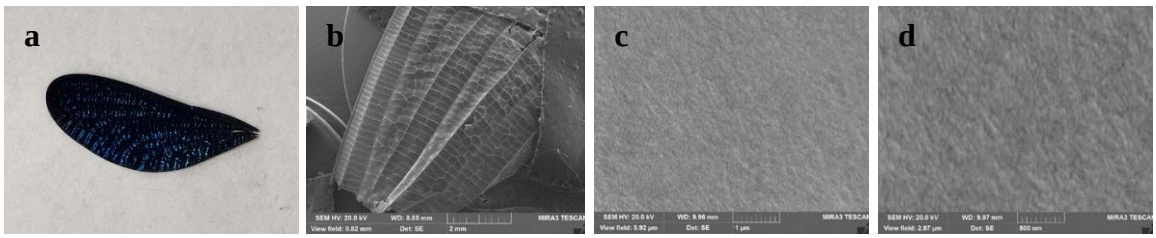

Figure 3.1.4 (a) Photograph of damselfly wing. **(b)** SEM image showing the nanoridges present on the damselfly wing after a thin layer of silver deposited taken at 20.0 kV- 50x: 100 nm Ag deposition. **(c)** SEM image showing the ridges present in the damselfly wing taken at 20.0 kV- 40kx: 100 nm Ag deposition**. (d)** SEM image of the damselfly wing taken at 20.0 kV- 80kx: 100 nm Ag deposition.

3.1.5 Japanese Rice Fish Scales

SEM image of the fish scales showed the gills present on the operculum of the fish in Figure 3.1.5b. The general view of the fish scales using the SEM showed tissues that are like short threads, protein structures called filaments. These filaments contain hollow photonic crystal fibres present in the operculum.[27] The studies on fish scales were discontinued midway through the experimentation because although there was a poor SERS signal present during analysis, this signal was irreproducible because of the irregular shaped fish scales present on the operculum. Hence, the fish scale substrates will not be commented on further in this thesis work.

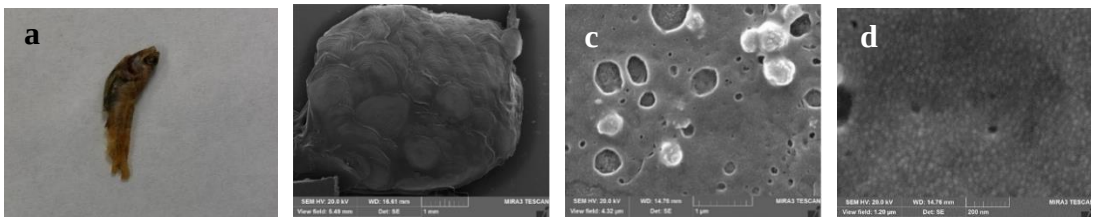

Figure 3.1.5 (a) Photograph of fresh water fish. **(b)** SEM image showing the circular-shaped fish scales after a thin layer of silver deposited taken at 20.0 kV- 50x: 100 nm Ag deposition. **(c)** SEM image showing the structure of a fish scale taken at 20.0 kV- 40kx: 100 nm Ag deposition. **(d)** SEM of the fish scale taken at 20.0 kV- 80kx: 100 nm Ag deposition.

3.1.6 Silver Film-Over-Nanospheres

Although SERS-active substrates have been fabricated by several innovative methods, vapour deposited metal film-over-nanospheres are among the most widely used substrates.[21] These substrates are commonly prepared from silver; however, other conductive metals such as gold and copper can also be investigated to determine the plasmonic system of metal nanoparticles. Copper serves as one of the more promising

ways to trap light and thereby achieve increased SERS enhancement using these SERS-active substrates. Plasmonic systems are based on particle-film plasmonic couplings which have recently attracted great attention because of the significantly enhanced electric field at the particle-film gaps.[47] When a metal film is deposited onto microscope slides with controllable particle-film gap distances, the FON system supports multiple plasmonic couplings from interparticle, particle-film and crevice gaps resulting in a large surface-enhanced Raman spectroscopy (SERS) effect.[31]

The periodicity in the structure of the FON substrates and the particle-film gaps greatly affects the surface plasmon resonances, and thus the SERS effects due to the interplay between multiple plasmonic couplings.[32] In line with this, silver film-over-nanospheres were prepared by initially drop-coating polystyrene sphere solution onto a coverslip and using the simple technique of physical vapour deposition to deposit a thin layer of silver onto the surface as depicted in Figure 3.1.6a. The characterization of the polystyrene coverslips was done using SEM. The surface structure of each coverslip was covered in a multilayer of polystyrene spheres that were well-defined across the coverslip. There was pronounced particle definition as the average diameter of the polystyrene spheres were found to be 678±5 nm using ImageJ software in Figure 3.1.6c.

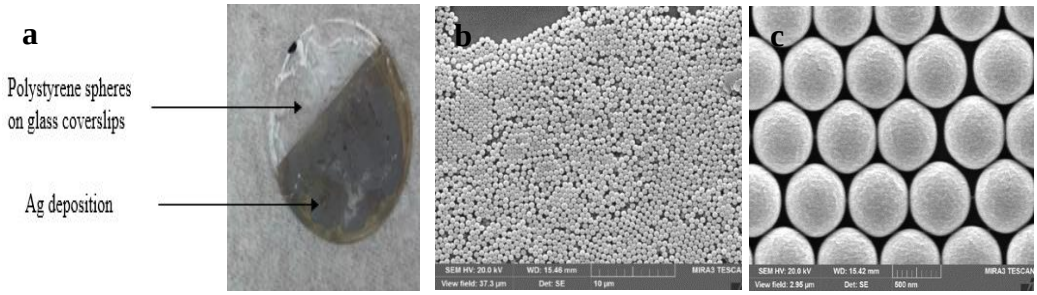

Figure 3.1.6: (a) Photograph of the coverslip after drop-coating 5 µL of 680 nm polystyrene sphere solution and the surface after a thin film of silver (Ag) was deposited using PVD. **(b)** SEM image showing the bilayer of polystyrene sphere solution on the coverslip at 20.0 kV- 40 kx. **(c)** SEM image showing polystyrene nanospheres on the surface of the coverslip taken at 20.0 kV- 80 kx: 100 nm Ag deposition.

3.2 SERS of Bioscaffolds

3.2.1 Comparison of Silver Film-Over-Nanospheres and Silver Island-Films

Silver island films (AgIF) with a varied thickness and coverage were prepared by depositing silver on a microscope slide by physical vapour deposition. The preparation of island-films as a SERS-active substrate was completed as a control as a visual comparison of the SERS intensity of different bioscaffolds and to determine whether the surface structure of the metal substrate was reproducible. The silver island-films assisted in determining the experimental conditions that affect the geometry and size of the silver particles. Using silver with the 780 nm laser line gave the best results in literature, which is why only those results are shown in this section.[24] One of the most common Raman reporter molecules is the simple thiol *para*-aminothiophenol (p-ATP), which is utilized in this thesis work to evaluate the SERS substrates. p-ATP was chosen as the Raman reporter because it adsorbs strongly to Ag and has a large spontaneous Raman cross-section.[48] As well as being an excellent Raman probe molecule, p-ATP undergoes

plasmon-assisted catalysis to 4,4'-dimercaptoaminobenzene (DMAB) which can be followed *in situ* using SERS.

This study was used to probe the three-dimensional nanostructure of SERS-active substrates and to compare the data with the enhancement properties of SERS-active substrates such as silver-island films and silver film-over-nanospheres. As shown in Figure 3.2.1; the SERS activity of the Ag deposited island-film showed no significant enhancement as compared to the nanostructured modification provided by the polystyrene nanospheres on the surface of the coverslips. The SEM image of the AgFON substrate (Figure 3.1.6c) shows a periodic metallic nanostructure with spherically arranged, close-packed arrays, where sharp crevice gaps are formed.

This huge improvement of SERS signal for the AgFON system when compared to the AgIF can be attributed to the additional electric-field enhancements from the particle−film and interparticle plasmon couplings when nanoparticles are assembled on the AgFON substrate.[35] The effect of an increase in field enhancements and the number of hot spots on the AgFON substrate can be clearly observed in the SERS spectra shown in Figure 3.2.1.

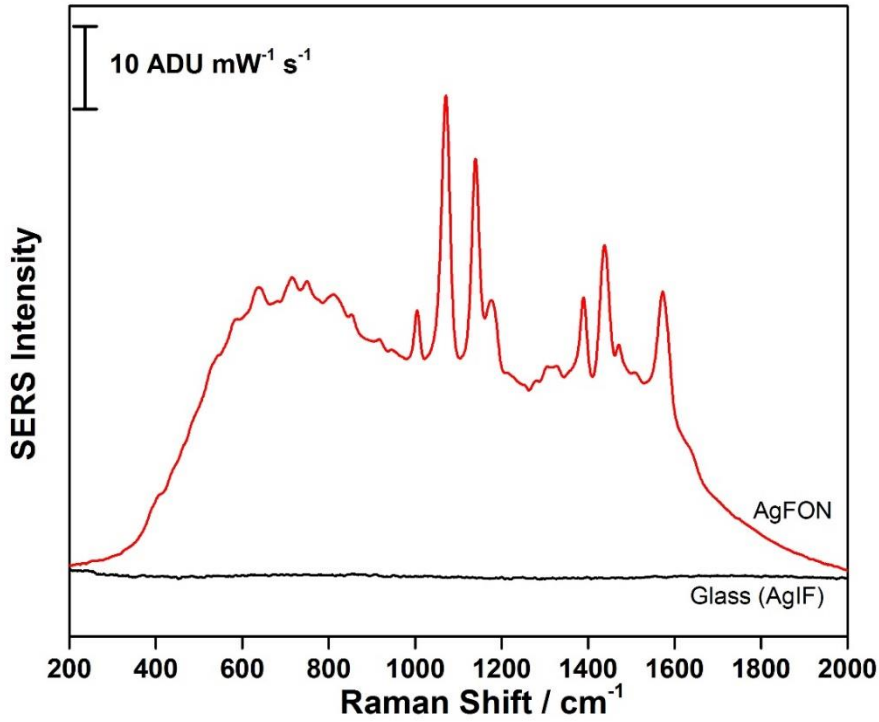

Figure 3.2.1: Average SERS spectra of p-ATP drop-coated on the silver film-over-nanospheres and silver island-film- 50 nm Ag deposition. (780 nm laser, 12.17 mW and acquisition time of 30 seconds)

With all the advantages offered by SERS, there is continuous need to explore different architectures that allow for the fabrication and use of a reproducible, uniformly enhancing SERS substrate. AgFON-based substrates have increased stability as compared to colloids, ease of fabrication, low cost, rapid fabrication, some tailoring of substrate architecture (shape, size, and coinage metal) to match plasmon bands with irradiation source, and good detection of analytes of interest commonly seen with silver-coated substrates.[47]

However, AgFON substrates are characterized as being highly irreproducible and having irregular arrayed nanostructure surfaces within a given area. This issue arises from

sphere packing where the main goal is to make well packed arrays of polystyrene nanospheres.[49] The volume of polystyrene sphere solution drop-coated on the coverslip and the swirling of the sphere solution across the coverslip has a big impact on the sphere packing. This leads to random overlapping of polystyrene spheres on the coverslip making it difficult to determine the arrangement of the spheres which in turn leads to insensitive SERS measurements.

In addition, using this type of fabrication process is not cost efficient, requires a great deal of effort, time and skill for fabrication, has a low sample collection efficiency, and does not necessarily result in a large uniform SERS active sensing area.[49] Considering the many issues still associated with SERS substrates, bioscaffolds offer a more sensitive, cost-efficient, reproducible, uniform and flexible substrate for SERS-sensing.

3.2.2 Comparison of Bioscaffolds based on SERS Signal

For each bioscaffold, 5 μL of a 1 mM solution of p-ATP was drop-coated onto the film of silver deposited onto the bioscaffold each with a varied silver thickness of 50 nm, 100 nm, 150 nm and 200 nm and allowed to dry in air. The study on fish scales were discontinued because of the irreproducibility of this SERS substrate. There was poor reproducibility as noted by the spot-to-spot variation of the Raman reporter (p-ATP) for ten randomly selected spots on the fish scale substrate indicated in Figure 3.2.2.1. A key challenge in acquiring high quality SERS signals for the fish scales was reducing the significant background fluorescence. This is believed to be due to an intrinsic fluorescence emanating from the fish scales.[50]

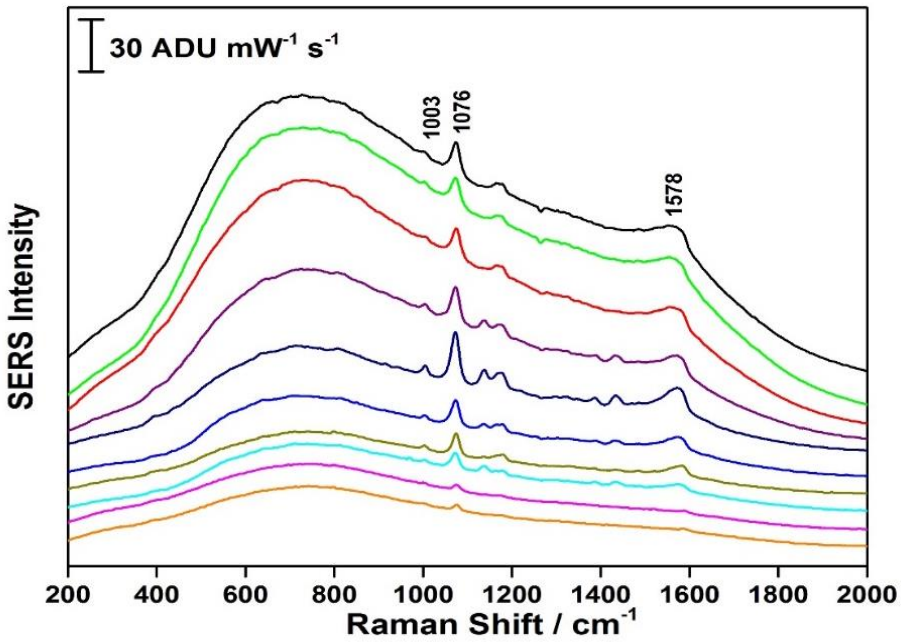

Figure 3.2.2.1: SERS spectra of p-ATP on fish scale- 50 nm Ag deposition. (780 nm laser, 12.17 mW and acquisition time of 30 seconds)

Initially, the blue mussel shell was considered the optimal substrate based on its obvious higher mechanical strength compared with other natural materials such as petals and butterfly wings. However, the crevices and cracks in the underlying structure of the blue mussel shell meant there were still pockets on the substrate that were unevenly coated in silver indicated by the high content of Ca as ($CaCO_3$) present in the EDX spectra in Figure 3.2.2.2. The Raman signal of the characteristic calcium carbonate at 1087 cm^{-1} and 1134 cm^{-1} from the blue mussel shell was easily identified in the SERS spectra for Figure 3.2.2.3. The high content of $CaCO_3$ in the mussel shell results in a weaker SERS sensitivity for the blue mussel shell when compared to the other bioscaffolds.

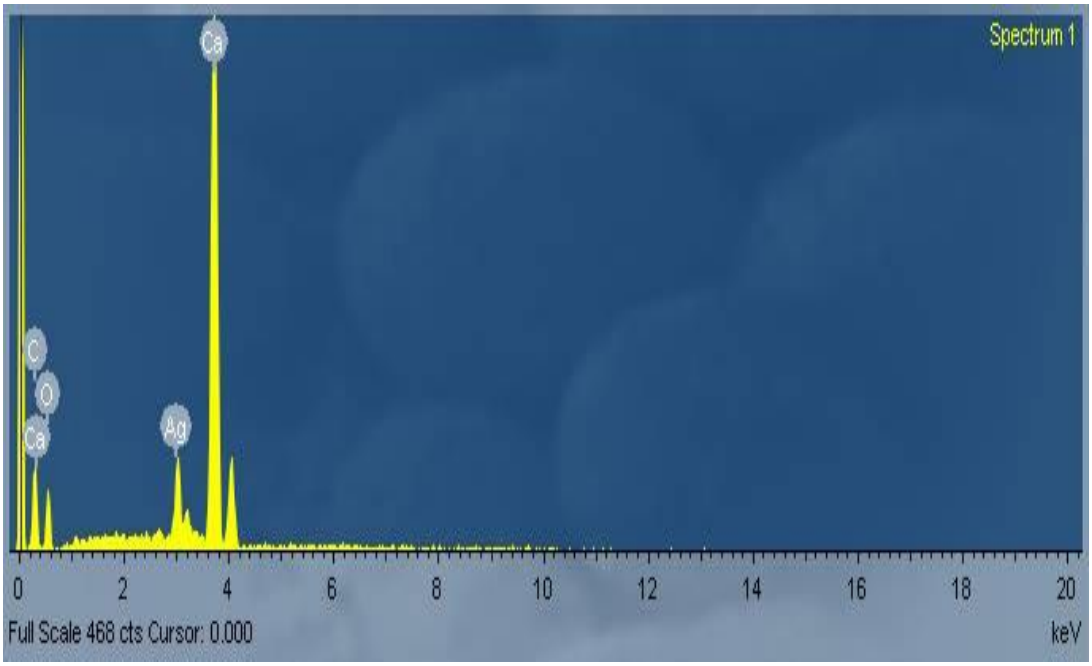

Figure 3.2.2.2: EDX spectra of blue mussel shell- 50 nm Ag deposition. (780 nm laser, 12.17 mW and acquisition time of 30 seconds)

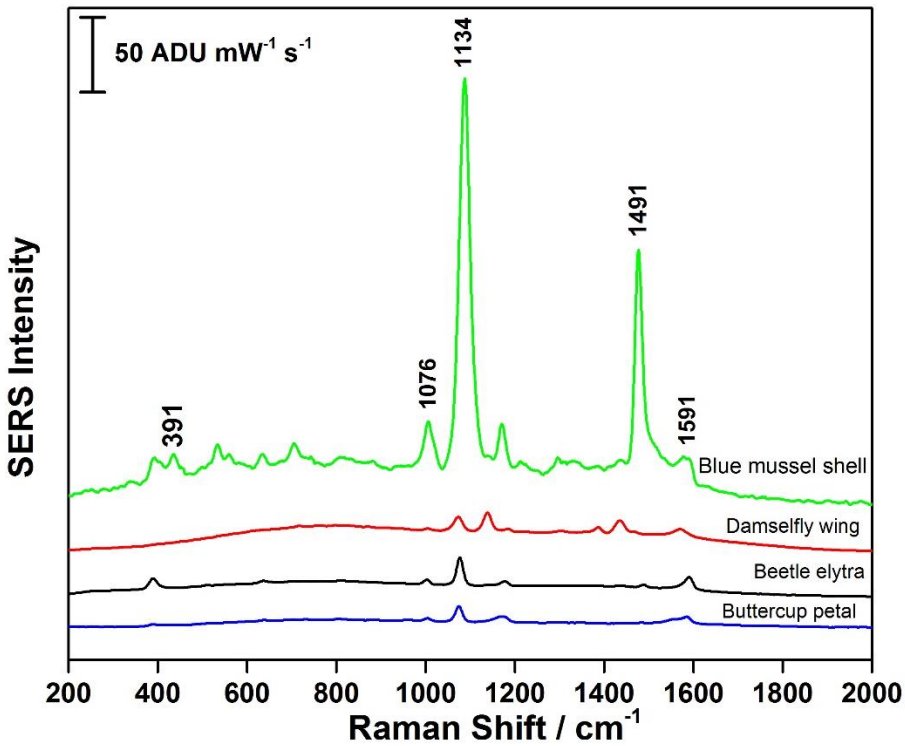

Figure 3.2.2.3: SERS spectra of p-ATP on each bioscaffold- 50 nm Ag deposition. (780 nm laser, 12.17 mW and acquisition time of 30 seconds)

In addition, the results showed excellent signal enhancement for the buttercup petals as indicated by the SERS spectra of p-ATP from in Figure 3.2.2.4. The beetle elytra were also used as a template because the outer wing is covered with regularly arranged protrusions as revealed by the SEM.[29] However, in the case of the beetle elytra when compared to the other bioscaffolds, the SERS intensity was significantly weaker except when 100 nm of silver was deposited on the surface as shown in Figure 3.2.2.4.

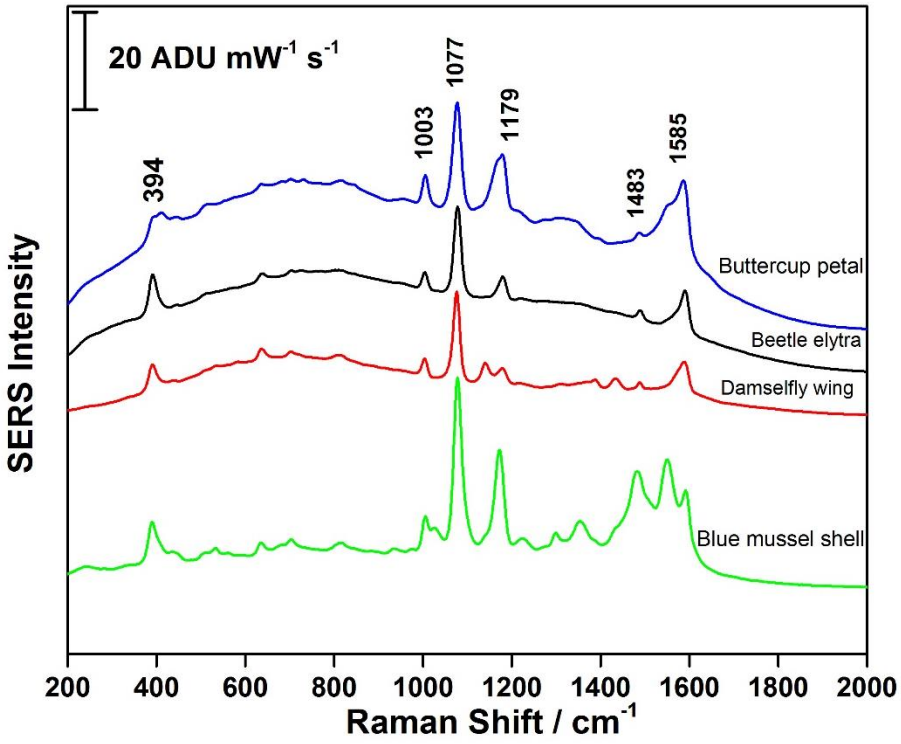

Figure 3.2.2.4: SERS spectra of p-ATP on each bioscaffold- 100 nm Ag deposition. (780 nm laser, 12.17 mW and acquisition time of 30 seconds)

The damselfly wings because of its periodic structure showed stable and reproducible spectra as indicated by the SERS spectra of the surface of the wing as shown

in Figure 3.2.2.5. The good uniformity and reproducibility over its entire area reduced the background component of the SERS spectra and it was able to reveal the spectral peaks that were previously hidden in the high background of SERS substrate measurements for the blue mussel shell. In addition, after depositing 150 nm of silver onto the surface of each bioscaffold, the SERS spectra in Figure 3.2.2.5 highlighted that the damselfly wing was the optimal substrate at that thickness and it should be mentioned that the damselfly wing displays apparent higher mechanical strength compared with the other natural materials such as the buttercup petal and is therefore a more durable SERS-active substrate.

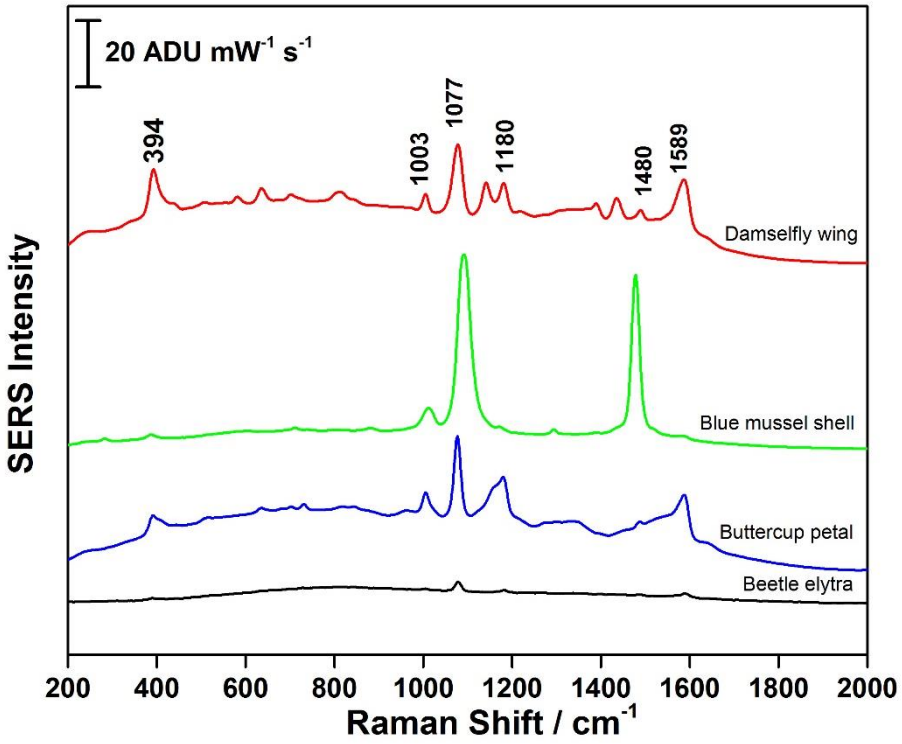

Figure 3.2.2.5: SERS spectra of p-ATP on each bioscaffold- 150 nm Ag deposition. (780 nm laser, 12.17 mW and acquisition time of 30 seconds)

The deposition of 150 nm of Ag showed the strongest SERS intensity which is due to the strong coupling effects between the Ag layer deposited on the surface of the nanostructured surface of the damselfly wing, beetle elytra and buttercup petal. These observations based on the SERS spectra highlights that the coupling effects between the Ag layer and the bioscaffolds are crucial to the improvement of SERS intensity. As the thickness of the Ag layer increased further, the Raman intensities became smaller as noted with each of the remaining substrates at 200 nm in Figure 3.2.2.6.

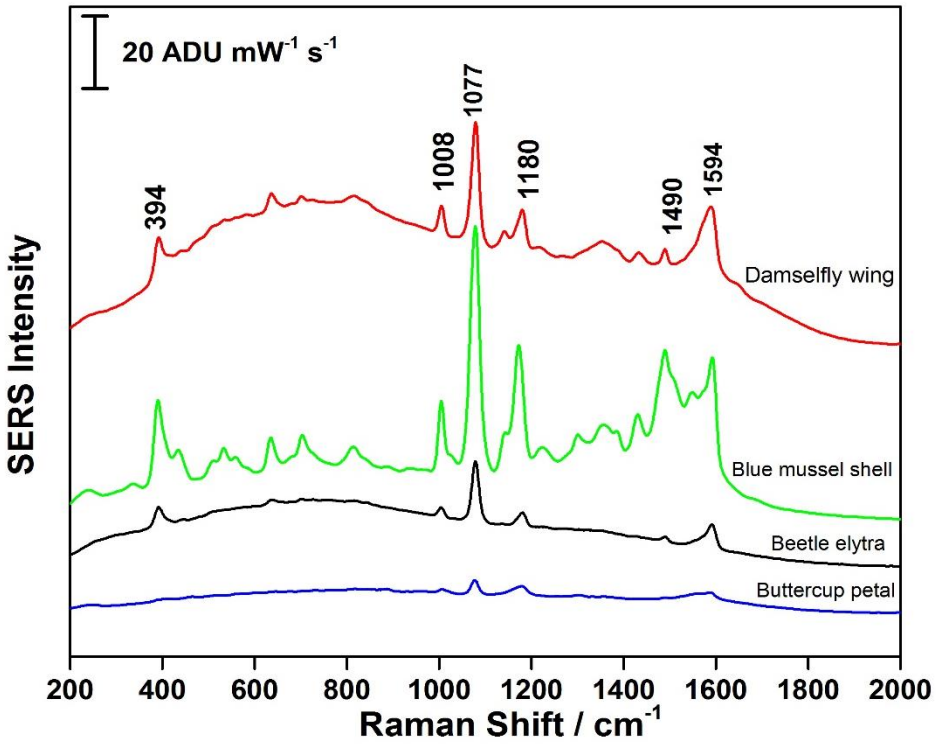

Figure 3.2.2.6: SERS spectra of p-ATP on each bioscaffold- 200 nm Ag. (780 nm laser, 12.17 mW and acquisition time of 30 seconds).

As the thickness of Ag increased, the gaps in-between the surface decreased. The decrease of gaps led to a weaker SERS signal because there was a loss of the nanostructured features at 200 nm of Ag. The thicker layer of Ag can become problematic

for sensitive SERS detection. This is because the silver is generally deposited effectively on the nanocavities and nanogaps of the bioscaffold and binds strongly to the surface and can therefore dominate the SERS signal and/or block surface access for target analytes. This work provides new insight with the use of the following bioscaffolds: buttercup petals, fish scales, damselfly wings, beetle elytra and blue mussel shells as an alternative substrate for the design and fabrication of three-dimensional SERS substrates.

3.2.3 Effect of Silver Film Thickness on SERS Signal

The surface of each bioscaffold presented an interesting morphology having reticular nanostructures in the case of the buttercup petals or circular nanostructures as shown with the beetle elytra.[51] The morphology of the damselfly wing contained nanostructured cavities along the wing. These multidimensional SERS-active substrates provide hot spots each having a strong local field enhancement. The first parameter adjusted for each bioscaffold was the thickness of silver deposited for the fabrication of SERS-active substrates in this experiment. The thickness varied from 50 nm, 100 nm, 150 nm and 200 nm on each bioscaffold namely blue mussel shell, beetle elytra, buttercup petal and damselfly wing. The reference spectra for each bioscaffold at each thickness from 50 nm to 200 nm can be found in the Appendix: Figure A1 through Figure A12.

Based on Figures 3.2.3.1 and Figure 3.2.3.2, it was determined that an increase in thickness for each bioscaffold eventually led to a decrease in SERS signal intensity. This was observed because an increased thickness causes the interparticle gaps present on the surface of the substrate to disappear completely.[24] It was further noted in the experiments

that the optimal thickness of silver deposited on the beetle elytra was 100 nm in Figure 3.2.3.1a. In Figure 3.2.3.1b, the optimal thickness of silver for the blue mussel shell was 200 nm. Likewise, for the buttercup petal, the optimum thickness deposited was 100 nm in Figure 3.2.3.2a and 150 nm for the damselfly wing according to Figure 3.2.3.2b.

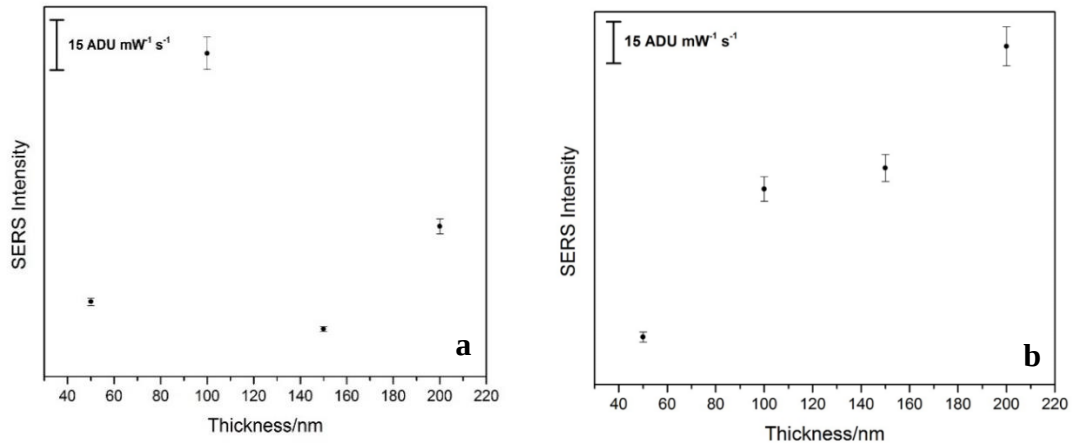

Figure 3.2.3.1 (a) SERS intensity of p-ATP (1080 cm^{-1}) on beetle elytra at different thickness of Ag deposition. **(b)** SERS intensity of p-ATP (1080 cm^{-1}) on blue mussel shell at different thickness of Ag deposition. (780 nm laser, 12.17 mW and acquisition time of 30 seconds).

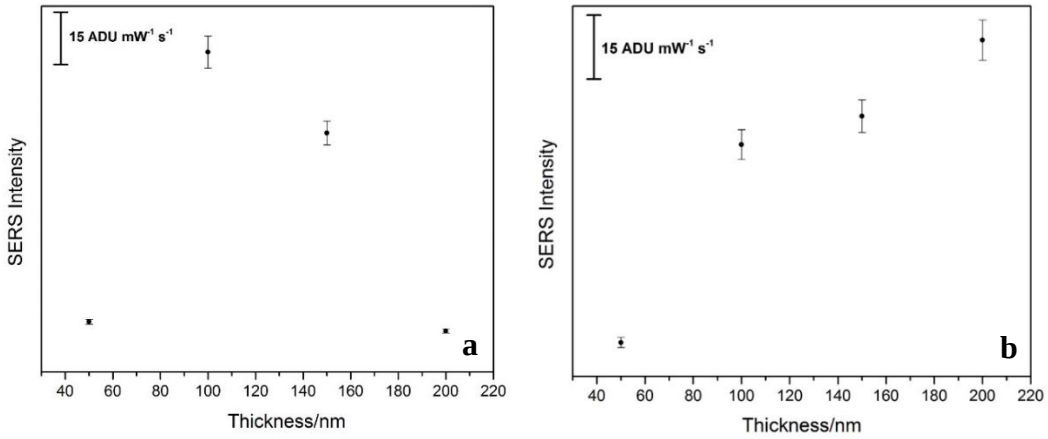

Figure 3.2.3.2 (a) SERS intensity of p-ATP (1080 cm^{-1}) on buttercup petal at different thickness of Ag deposition. **(b)** SERS intensity of p-ATP (1080 cm^{-1}) on damselfly wing at different thickness of Ag deposition. (780 nm laser, 12.17 mW and acquisition time of 30 seconds).

After determining the optimal thickness for each bioscaffold, the coefficient of variation shown in Table 3.2.3 was important to measure the relative variability in the SERS signal for each bioscaffold for the 1080 cm^{-1} peak of p-ATP. The coefficient of variation is calculated by dividing the standard deviation of the sample set by the mean and this allowed for the comparison between each bioscaffold set based on metal thickness on the surface. The bioscaffold with the lowest spot-to-spot variation at 150 nm was the buttercup petal and damselfly wing at 9% and 35% respectively. As a result, further optimization was undertaken for the buttercup petal and damselfly wing. The relatively high coefficient of variation for the beetle elytra in Table 3.2.3 made it an unsuitable SERS-active substrate. The coefficient of variation for the beetle elytra varied from 31% to 72% and there was poor signal reproducibility at each thickness as shown previously by the high spot-to-spot variation in the SERS spectra.

Table 3.2.3: Coefficient of variation for each bioscaffold calculated using 1080 cm^{-1} peak for p-ATP. The deposition thickness was varied using physical vapour deposition.

Coefficient of variation (%)			
Thickness (nm)	Bioscaffold		
	Buttercup petal	Beetle elytra	Damselfly wing
50	30	32	42
100	41	71	55
150	9	45	35
200	16	31	77

3.3 Deposition Parameter Changes for Bioscaffolds

After evaluating the fabrication method of multidimensional SERS-active substrates and agreeing on a suitable silver film thickness of 150 nm, the following deposition parameters were further investigated: rotation speed, deposition time and current. The coefficient of variation for each bioscaffold allowed for a quantitative detection method to determine which parameter played a centrally important role in determining the uniform coating of the final deposit on the buttercup petal and the damselfly wing. In Figure 3.3.1.1, the rotation speed of the damselfly wing was set to the lowest at 50 rpm as compared to Figure 3.3.1.3 where the rotation speed was set to the highest at 80 rpm. The change in rotation speed significantly affected the coefficient of variation for the damselfly wing according to Table 3.3.1. The lowest coefficient of variation (CV) was determined to be 15%, at 80 rpm, which provided a reproducible SERS spectrum for p-ATP at the observed peaks at 1006, 1080 and 1590 cm^{-1}. On the other hand, at the lowest rotation speed, the spot to spot variation was high at 92% indicated by the spectrum in Figure 3.3.1.1.

For the buttercup petal, rotation had an opposite effect because the lower CV was determined to be 16% at 50 rpm, which provided a reproducible SERS spectrum for p-ATP at the observed peaks at 1006, 1080 and 1590 cm^{-1} in Figure 3.3.1.5. The spot to spot variation was high at 67% at a rotation speed of 80 rpm as shown in Figure 3.3.1.7 further highlighting that the rotation speed of the substrate holder is very important for metal deposition because the deposition thickness is approximately proportional to the inverse square root of the rotation speed. As the different bioscaffolds are concerned, it appears, in general, that the rotation speed of the substrate holder is less reproducible in

the case of the damselfly wing. As the rotation speed increased, this led to better SERS results for the damselfly wing in Table 3.3.1. This is likely related to the higher surface area and the many horizontal protrusions present in the damselfly wing.

3.3.1 Parameter Change: Substrate Rotation

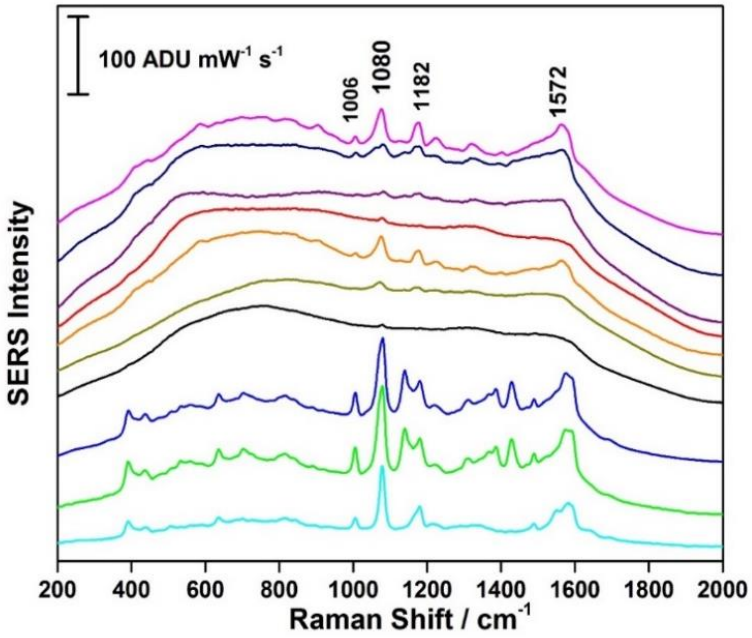

Figure 3.3.1.1: SERS spectra of p-ATP on damselfly wing- 50 rpm. (780 nm laser, 12.17 mW and acquisition time of 30 seconds).

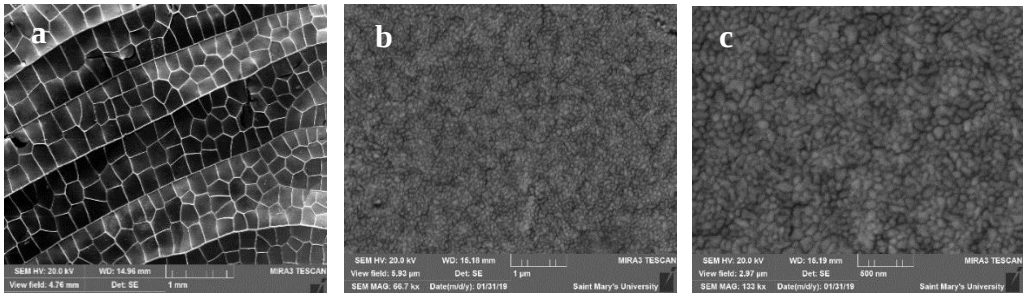

Figure 3.3.1.2: (a) SEM image showing surface of the damselfly wing- 50 rpm taken at 20.0 kV- 50x. **(b)** SEM image showing the surface of the damselfly wing- 50 rpm taken at 20.0 kV- 40 kx: **(c)** SEM image showing the surface of the damselfly wing- 50 rpm taken at 20.0 kV- 80 kx: 150 nm Ag deposition.

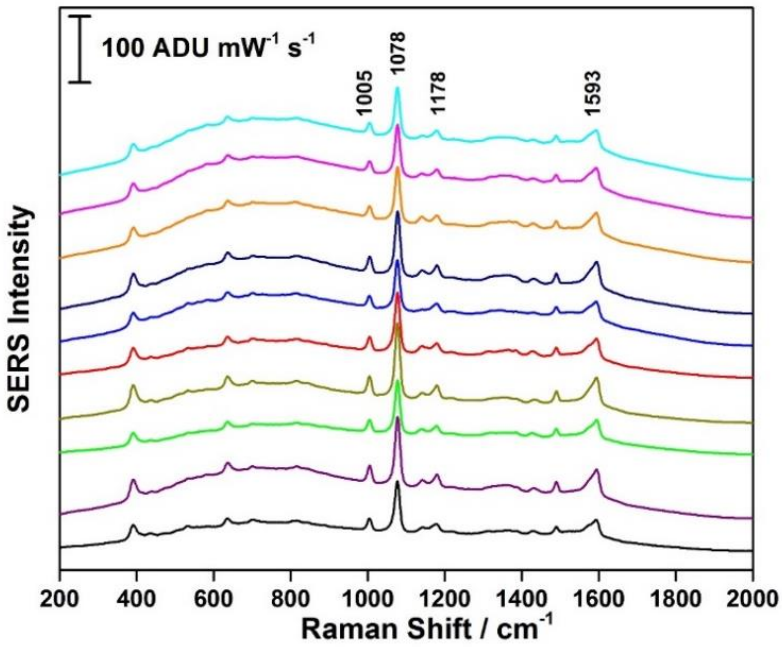

Figure 3.3.1.3: SERS spectra of p-ATP on damselfly wing- 80 rpm. (780 nm laser, 12.17 mW and acquisition time of 30 seconds).

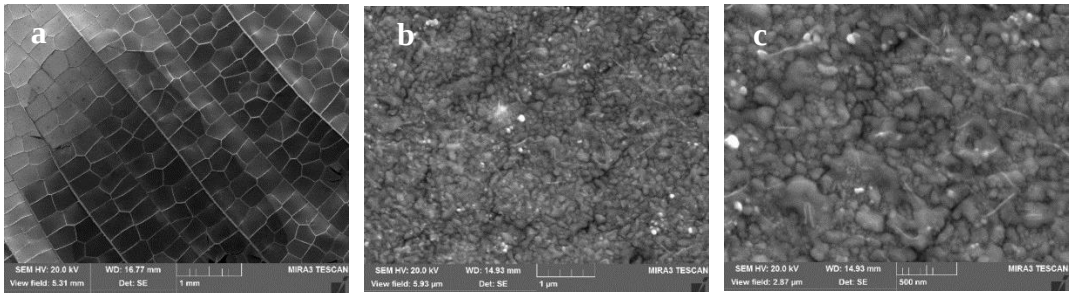

Figure 3.3.1.4: (a) SEM image showing surface of the damselfly wing- 80 rpm taken at 20.0 kV- 50x. . **(b)** SEM image showing the surface of the damselfly wing-80 rpm taken at 20.0 kV- 40 kx: **(c)** SEM image showing the surface of the damselfly wing-80 rpm taken at 20.0 kV- 80 kx: 150 nm Ag deposition.

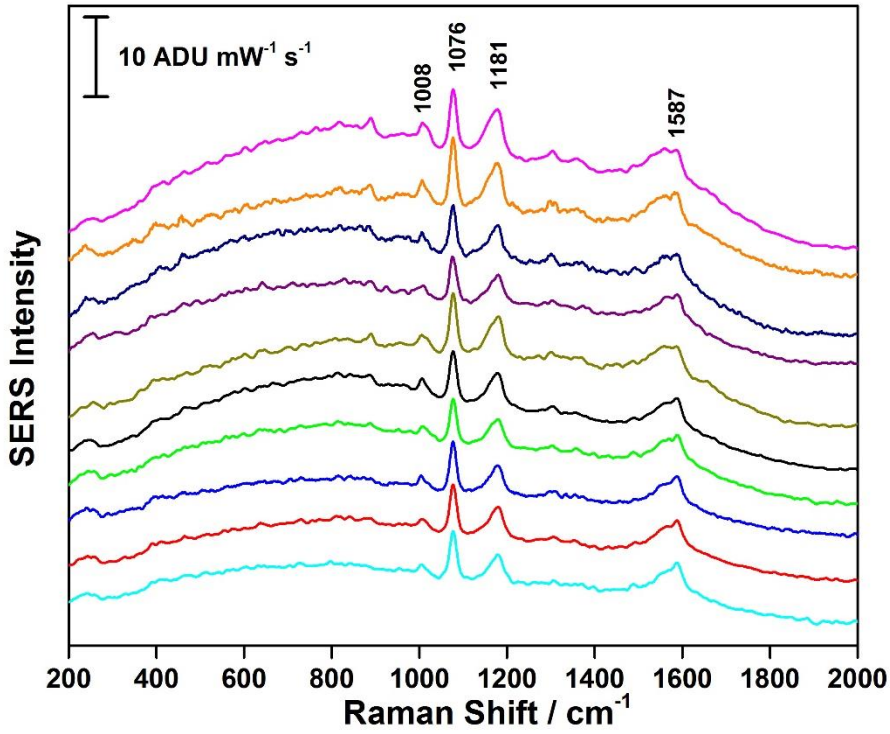

Figure 3.3.1.5: SERS spectra of p-ATP on buttercup petal- 50 rpm. (780 nm laser, 12.17 mW and acquisition time of 30 seconds).

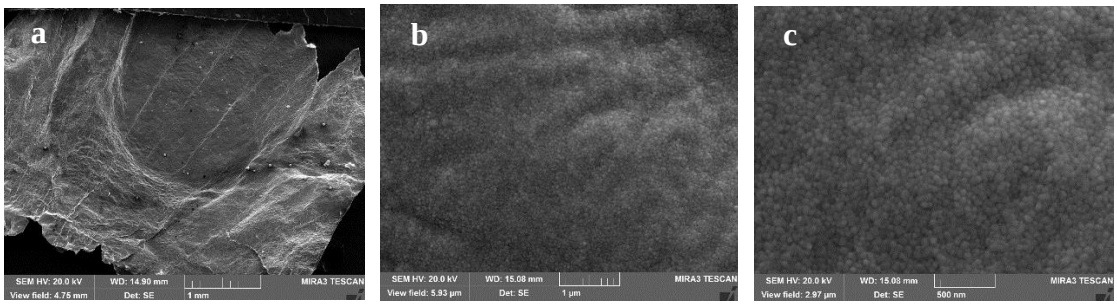

Figure 3.3.1.6: (a) SEM image showing surface of the buttercup petal- 50 rpm taken at 20.0 kV- 50x. . **(b)** SEM image showing the surface of the buttercup petal- 50 rpm taken at 20.0 kV- 40 kx: **(c)** SEM image showing the surface of the buttercup petal- 50 rpm taken at 20.0 kV- 80 kx: 150 nm Ag deposition.

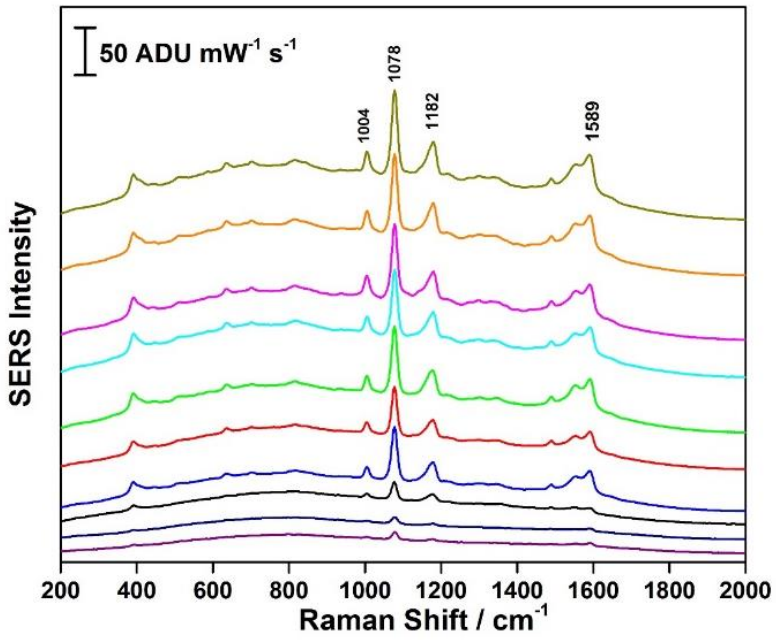

Figure 3.3.1.7: SERS spectra of p-ATP on buttercup petal- 80 rpm. (780 nm laser, 12.17 mW and acquisition time of 30 seconds).

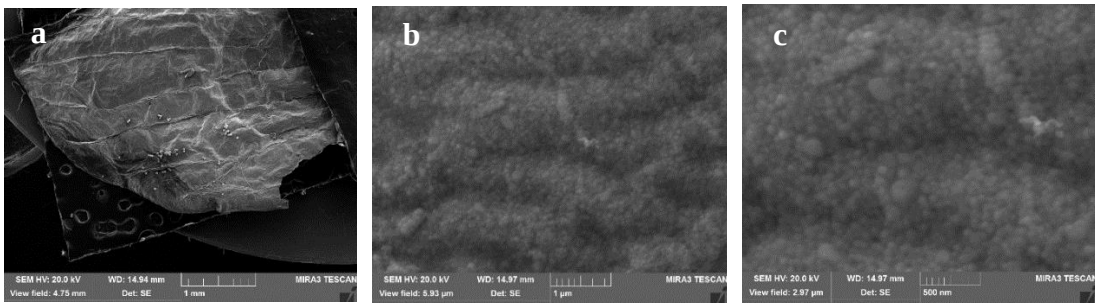

Figure 3.3.1.8: (a) SEM image showing surface of the buttercup petal- 80 rpm taken at 20.0 kV- 50x. . **(b)** SEM image showing the surface of the buttercup petal- 80 rpm taken at 20.0 kV- 40 kx: **(c)** SEM image showing the surface of the buttercup petal- 80 rpm taken at 20.0 kV- 80 kx: 150 nm Ag deposition.

3.3.2 Parameter Change: Deposition Rate

In Figure 3.3.2.1, the deposition rate of the buttercup petal was set to 1.00 Å/s and the CV was determined to be 9%, which provided a reproducible SERS spectrum for p-ATP. The change in deposition rate to 4.00 Å/s on the buttercup petal made it impossible to obtain decent SERS spectra because there was too much background noise present in the SERS signal. This was also noticed for damselfly wing at 1.00 Å/s which made it difficult to obtain decent SERS spectra. For the damselfly wing, the deposition rate at 4.00 Å/s provided a much higher CV which was determined to be 66% showing significant spot to spot variation as shown in Figure 3.3.2.3.

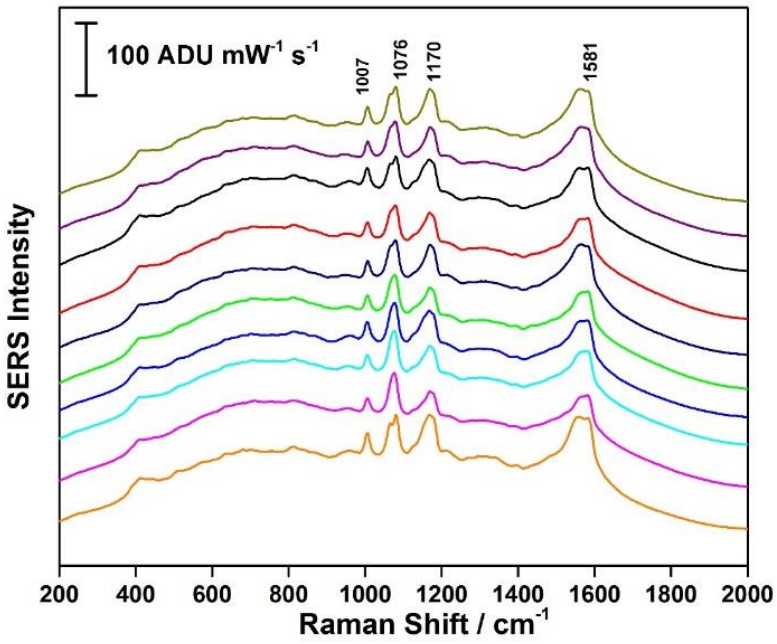

Figure 3.3.2.1: SERS spectra of p-ATP on buttercup petal- 1.00 Å/s. (780 nm laser, 12.17 mW and acquisition time of 30 seconds).

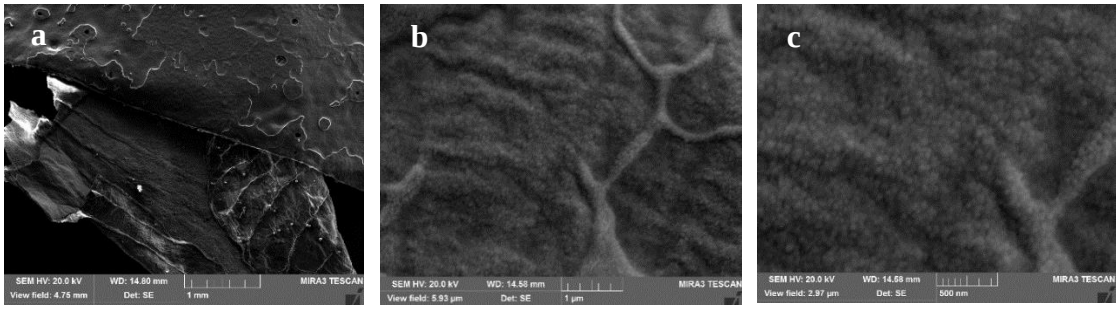

Figure 3.3.2.2: (a) SEM image showing surface of the buttercup petal- 1.00 Å/s taken at 20.0 kV- 50x. . **(b)** SEM image showing the surface of the buttercup petal- 1.00 Å/s taken at 20.0 kV- 40 kx: **(c)** SEM image showing the surface of the buttercup petal- 1.00 Å/s taken at 20.0 kV- 80 kx: 150 nm Ag deposition.

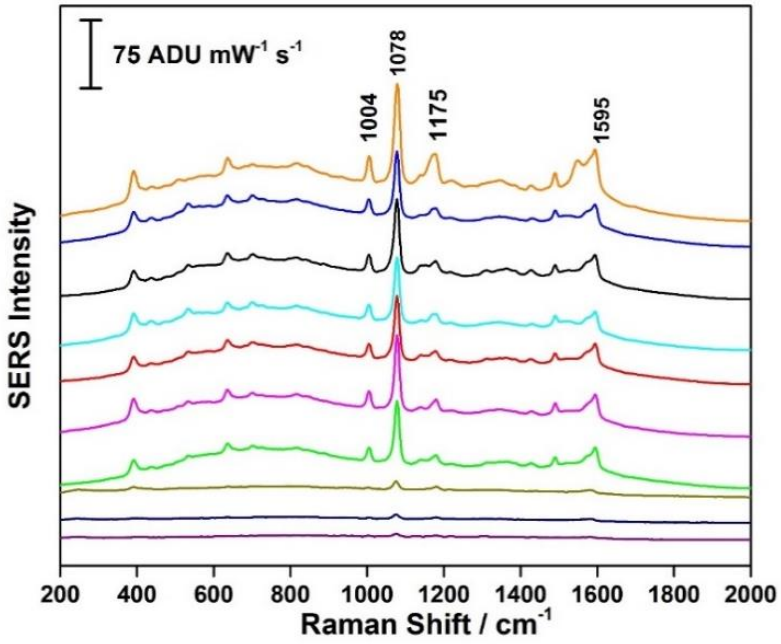

Figure 3.3.2.3: SERS spectra of p-ATP on damselfly wing- 4.00 Å/s deposition using the 780 nm laser. (12.17 mW and acquisition time of 30 seconds).

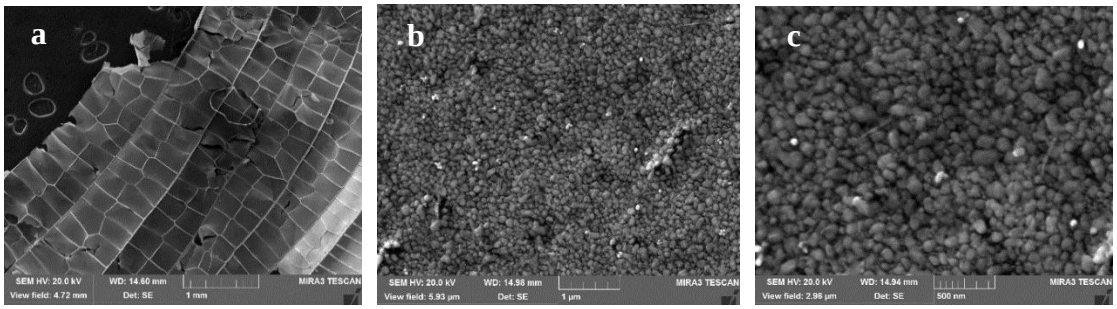

Figure 3.3.2.4: (a) SEM image showing surface of the damselfly wing- 4.00 Å/s taken at 20.0 kV- 50x. . **(b)** SEM image showing the surface of the damselfly wing- 4.00 Å/s taken at 20.0 kV- 40 kx: **(c)** SEM image showing the surface of the damselfly wing- 4.00 Å/s taken at 20.0 kV- 80 kx: 150 nm Ag deposition

3.3.3 Parameter Change: Current

In Figure 3.3.3.1, the change in current at 2.5 A accounted for no significant effect in the coefficient of variation for the damselfly wing at a change in current at 10 A as

shown in Figure 3.3.3.3. The results were also similar for both Figure 3.3.3.5 and Figure 3.3.3.7, for the buttercup petal whereby changing the current from 2.5 A to 10 A had no significant effect regarding the metal deposition on each surface.

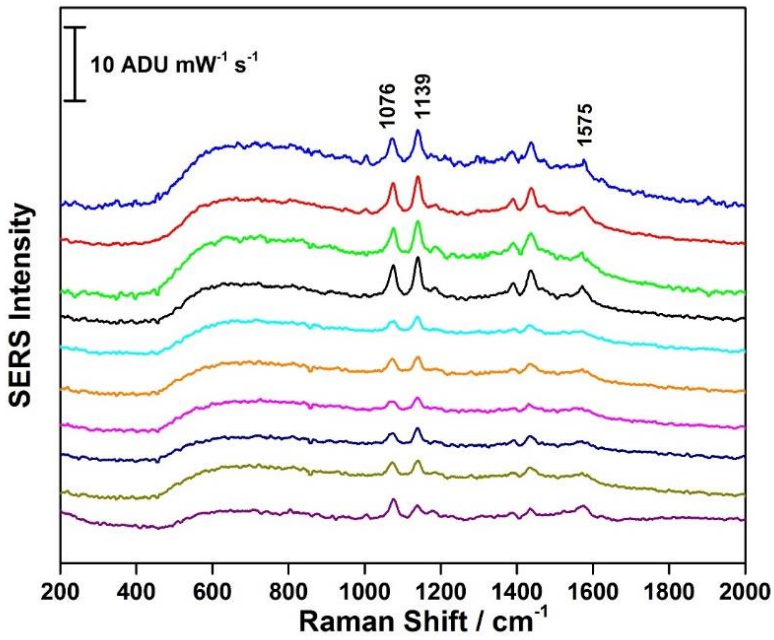

Figure 3.3.3.1: SERS spectra of p-ATP on damselfly wing- 2.5 A. (780 nm laser, 12.17 mW and acquisition time of 30 seconds)

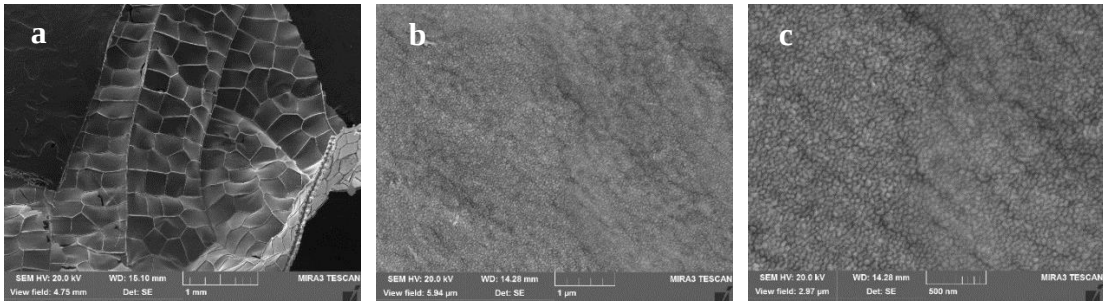

Figure 3.3.3.2: (a) SEM image showing surface of the damselfly wing- 2.5 A taken at 20.0 kV- 50x. . **(b)** SEM image showing the surface of the damselfly wing- 2.5 A taken at 20.0 kV- 40 kx: **(c)** SEM image showing the surface of the damselfly wing- 2.5 A taken at 20.0 kV- 80 kx: 150 nm Ag deposition

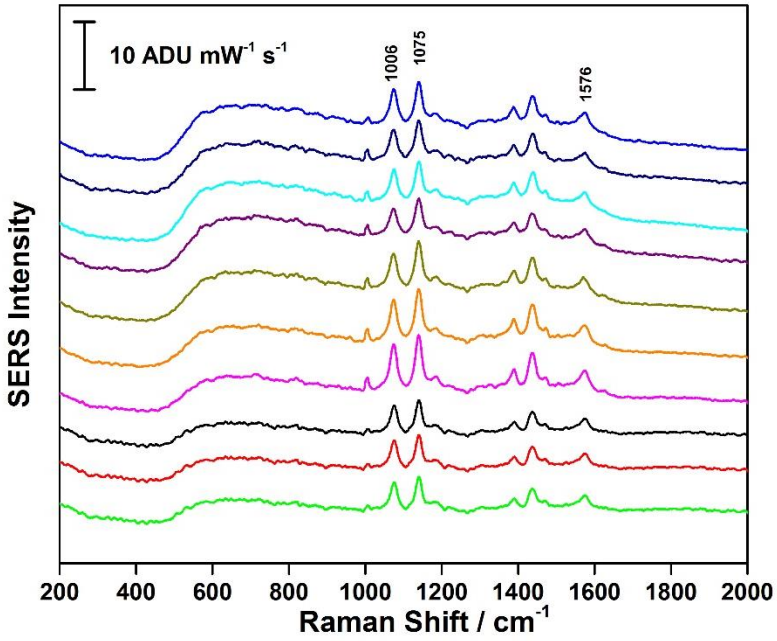

Figure 3.3.3.3: SERS spectra of p-ATP on damselfly wing- 10 A. (780 nm laser, 12.17 mW and acquisition time of 30 seconds)

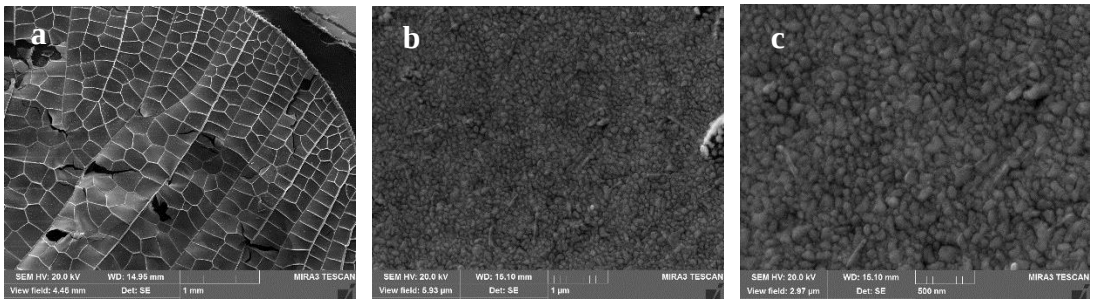

Figure 3.3.3.4: (a) SEM image showing surface of the damselfly wing- 10 A taken at 20.0 kV- 50x. . **(b)** SEM image showing the surface of the damselfly wing- 10 A taken at 20.0 kV- 40 kx: **(c)** SEM image showing the surface of the damselfly wing- 10 A taken at 20.0 kV- 80 kx: 150 nm Ag deposition

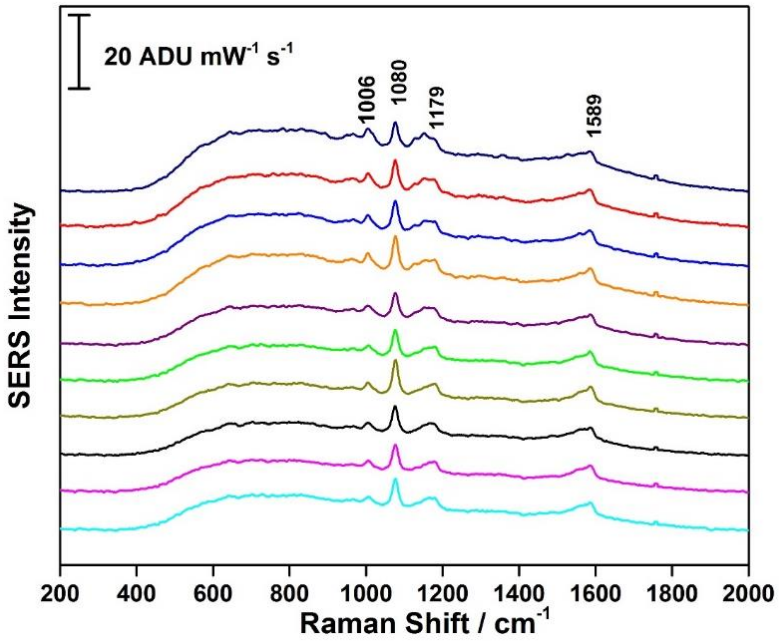

Figure 3.3.3.5: SERS spectra of p-ATP on buttercup petal- 2.5 A. (780 nm laser, 12.17 mW and acquisition time of 30 seconds).

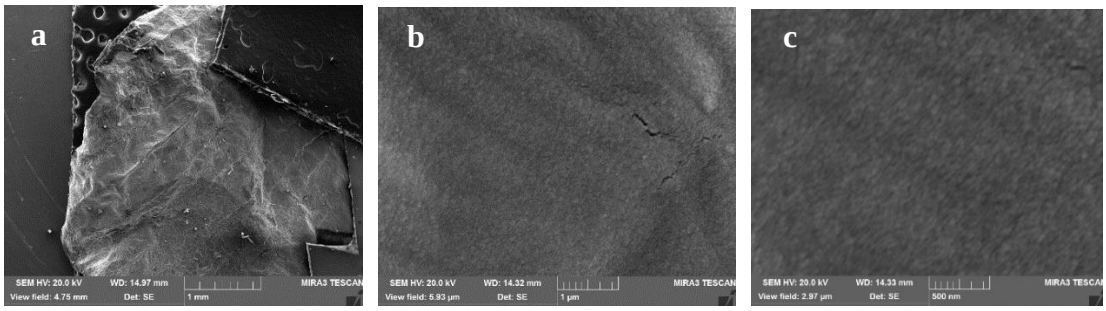

Figure 3.3.3.6: (a) SEM image showing surface of the buttercup petal- 2.5 A taken at 20.0 kV- 50x. . **(b)** SEM image showing the surface of the buttercup petal- 2.5 A taken at 20.0 kV- 40 kx: **(c)** SEM image showing the surface of the buttercup petal- 2.5 A taken at 20.0 kV- 80 kx: 150 nm Ag deposition.

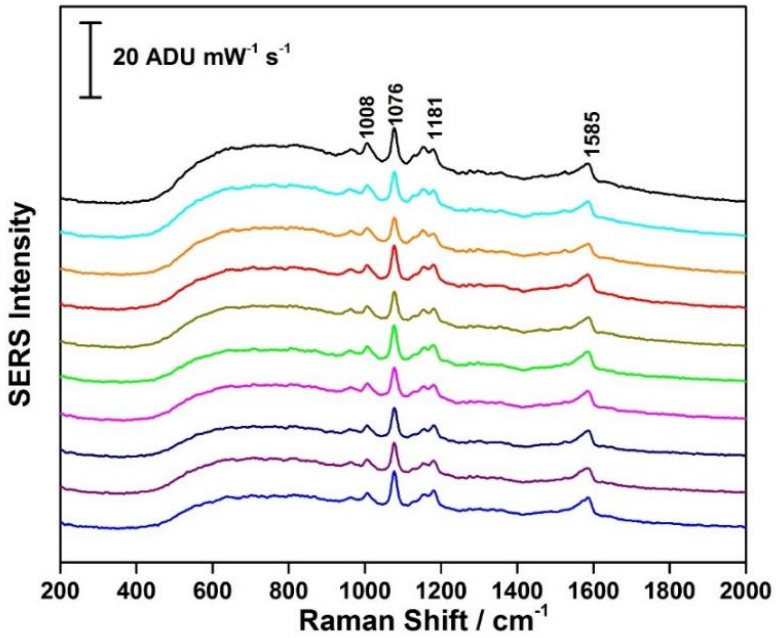

Figure 3.3.3.7: SERS spectra of p-ATP on buttercup petal- 10 A. (780 nm laser, 12.17 mW and acquisition time of 30 seconds).

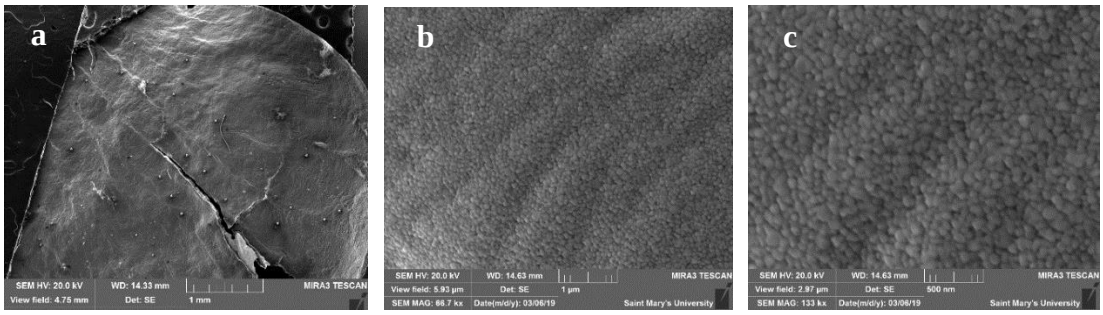

Figure 3.3.3.8: (a) SEM image showing surface of the buttercup petal- 10 A taken at 20.0 kV- 50x. . **(b)** SEM image showing the surface of the buttercup petal- 10 A taken at 20.0 kV- 40 kx: **(c)** SEM image showing the surface of the buttercup petal- 10 A taken at 20.0 kV- 80 kx: 150 nm Ag deposition.

Table 3.3.1: Coefficient of variation for ideal bioscaffolds using 1080 cm^{-1} peak of p-ATP. The manipulated physical vapour deposition parameters include deposition rate, rotation speed and current.

Coefficient of variation (%)		
Parameters	Bioscaffold	
Deposition Rate (Å/s)	Buttercup petal	Damselfly wing
1.00	9	N/A
2.00	9	45
4.00	N/A	66
Rotation speed (rpm)	Buttercup petal	Damselfly wing
50	16	92
65	9	45
80	67	15
Current (A)	Buttercup petal	Damselfly wing
2.5	14	50
5.0	9	45
10.0	13	24

It must be noted that the studies for the damselfly wing at 1.00 Å/s and the buttercup petal at 4.00 Å/s was not available due in part to the fact that there was no SERS signal present for the spectra at these deposition parameters except for background fluorescence and noise for each spectra. The reference spectra for each bioscaffold at deposition parameter change can be found in the Appendix: Figure A13 through Figure A20. The change in deposition rate had a significant effect on the spot-to-spot variation for the buttercup petal which had the lowest coefficient of variation of 9% in Table 3.3.1 at a deposition rate of 1.00 Å/s according to Figure 3.3.2.1 and it was impossible to obtain

a decent SERS signal at 4.00 Å/s. In contrast, at a deposition rate of 4.00 Å/s for the damselfly wing in Figure 3.3.2.3, the coefficient of variation was 66% as shown in Table 3.3.1 but it was also difficult to obtain decent SERS spectra at a deposition rate of 1.00 Å/s for the damselfly wing. The deposition rate influences the crystal structure of deposited films on the bioscaffold. The lower deposition rate of 1.00 Å/s with the buttercup petal not only affected the metal film growth on the buttercup petal but the amount of pure metal deposited on the surface increased.

On the other hand, the thicker layer on the damselfly wing made it more difficult for SERS analysis and the characteristic peaks. The results indicated that the adhesion strength of the pure metal decreased with increasing thickness of the initial film for the damselfly wing. In Figure 3.3.3.1, the change in current accounted for no significant effect in the coefficient of variation for the damselfly wing. The results were the same for both Figure 3.3.3.3 and Figure 3.3.3.5, for the buttercup petal whereby changing the current from 2.5 A to 10 A had no significant effect regarding the metal deposition on each surface. The assumption was that increasing the current throughout the unit would trigger the growth of the metal deposits on the surface of the damselfly wing and the buttercup petal.

In summary, the deposition parameters not only influenced the adhesion strength of the silver films and the bioscaffold but determined the particle size of the silver films. In comparison to AgFONs, it was shown in this thesis work that bioscaffolds can be exploited for next generation plasmonic substrates as shown in Figure 3.3.3.7. The damselfly wing and buttercup petal show great promise as SERS-active substrates from

both the point of view of sustainability as well as performance as the p-ATP signal was more intense for the SERS spectra in Figure 3.3.3.7.

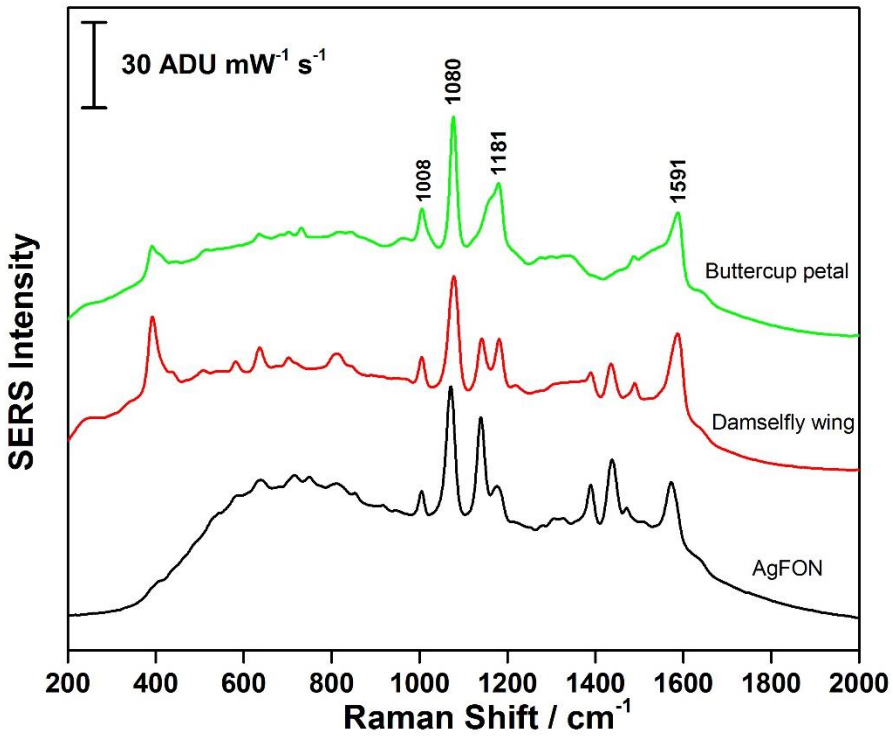

Figure 3.3.3.9: SERS spectra of p-ATP on buttercup petal, damselfly wing and AgFON. (780 nm laser, 12.17 mW and acquisition time of 30 seconds).

In this way, multidimensional architectures can be fashioned using natural materials such as damselfly wings and buttercup petals. The final optimized conditions for the bioscaffolds: the buttercup petal and the damselfly wing were a thickness of 150 nm, deposition rate of 2.00 Å/s, substrate rotation at 65 rpm and the ideal current was 5 A. The damselfly wing and buttercup petal substrates produced through physical vapour deposition were very promising, showing excellent SERS activity and less background fluorescence in comparison to the traditional AgFON substrates.

Chapter 4: Conclusion

This honours thesis work explored the use of bioscaffolds for the fabrication of multidimensional SERS substrates. Substrates were deposited with silver using the PVD unit and parameters such as power, current, thickness, rotation speed and deposition rate were varied. It was determined that varying the parameters was necessary to achieve good SERS signal intensity. The use of AgIFs and AgFONs as SERS-active substrates was successfully demonstrated, however the SERS spectra showed significant spot-to-spot variation across the substrate. The results of the SERS studies for the buttercup petal, damselfly wing and beetle elytra showed that the SERS spectrum could be greatly improved by using a thickness of 150 nm of silver on the surface of each substrate. The SERS spectra obtained for each bioscaffold were shown to be attributed to the Raman reporter p-ATP and the buttercup petal was found to be the most ideal substrate of the five selected, providing reproducible and sensitive SERS spectra for p-ATP. As a result, it is fair to say that this thesis work offered a new multidimensional bioscaffold for SERS detection by improving signal intensity and highlighting the opportunity of using novel, recyclable substrates to improve upon the already promising method of SERS-active substrates by using PVD.

Chapter 5: Future Work

In future, the deposition of copper onto the ideal bioscaffold for SERS detection can be used to reduce reliability on the high cost and less earth abundant Ag metal. Cu is an excellent alternative metal but suffers from ease of oxidation and a lack of reported nanostructures. In light of this, the creation of a novel type of Cu SERS-active bioscaffold provides an easier method to fabricate copper nanoparticles because current wet chemical methods remain elusive. Moreover, surface modifications to the bioscaffold by the addition of surfactants can be explored to achieve better adhesion between the deposited metal and the nanostructures present in the substrate.

SERS substrates need to be further optimized such that routine detection of a range of molecules can be detected. By using this novel, recyclable substrate an important goal for this thesis work is the application of these multidimensional SERS-active substrates to detect atrazine. The real-life impact of this work can be used to detect atrazine which has been associated with low fetal weight, heart and urinary defects in humans.[52] Based on this work, it is possible to functionalize multidimensional SERS-active substrates for rapid and on-site detection of food and water samples. In addition, other bioscaffolds should be evaluated, such as peacock feathers, which have structural colour and are renewable, as well as green seaweed, which have nanoscale features in the chloroplasts.

Chapter 6: References

1. Kneipp, K.; Kneipp, H.; Itzkan, I.; Dasari, R. R.; Feld, M. S. *J. Phys.Condensed Mat.* **2002**, *14*, R597-R624.

2. Jeanmaire, D. L.; Van Duyne, R. P. *J. Electroanal. Chem. Int. Electrochem.* **1977**, *84*, 1-20.

3. Creighton, J.; Albrecht, M.; Hester, R.; Matthew, J. *Chem. Phys. Lett.* **1978**, *55*, 55-58.

4. Sharma, B.; Frontiera, R. R.; Henry, A. I.; Ringe, E.; Van Duyne, R. P. SERS: Materials, applications, and the future. *Mater. Today*, **2012**, 15, 16-25.

5. Oh, Y.; Kang, M.; Park, M.; Jeong, K. Engineering Hot Spots on Plasmonic Nanopillar Arrays for SERS: A Review. *Biochip Journal* **2016**, *10*, 297-309

6. Zhang, M.; Meng, J.; Wang, D.; Tang, Q.; Chen, T.; Rong, S.; Liu, J.; Wu, Y. Biomimetic synthesis of hierarchical 3D Ag butterfly wing scale arrays/graphene composites as ultrasensitive SERS substrates for efficient trace chemical detection. *J. Mater. Chem. C* **2018**, *6*, 1933-1943.

7. Zhou, H.; Fan, T.; Zhang, D. *Chemsuschem* **2011**, *4*, 1344-1387.

8. Yang, J.; Zhen, L.; Ren, F.; Campbell, J.; Rorrer, G. L.; Wang, A. X. *J. Biophotonics* **2015**, *8*, 659-667.

9. Kahraman, M.; Mullen, E. R.; Korkmaz, A.; Wachsmann-Hogiu, S. Fundamentals and applications of SERS-based bioanalytical sensing. *Nanophotonics* **2017**, *6*, 831-852

10. Rycenga, M.; Cobley, C.M.; Zeng, J.; Li, W.; Moran, C. H.; Zhang, Q.; Qin, D.; Xia, Y. *Chem Rev*. **2011**, 111, 3669-3712.

11. Tan, H.; Santbergen, R.; Smets, A. H. M.; Zeman, M. Plasmonic Light Trapping in Thin-film Silicon Solar Cells with Improved Self-Assembled Silver Nanoparticles. *Nano Lett.* **2012**, *12*, 4070-4076.

12. Wang, Y.; Wang, M.; Sun, X.; Shi, G.; Zhang, J.; Ma, W.; Ren, L. Grating-like SERS substrate with tunable gaps based on nanorough Ag nanoislands/moth wing scale arrays for quantitative detection of cypermethrin. *Opt. Express* **2018**, *26*, 22168-22181.

13. He, J.; Shen, Q.; Yang, S.; He, G.; Tao, P.; Song, C.; Wu, J.; Deng, T.; Shang, W. Coupling effects in 3D plasmonic structures templated by Morpho butterfly wings. *Nanoscale* **2018**, *10*, 533-537.

14. Mendes, M. J.; Morawiec, S.; Crupi, I.; Simone, F.; Priolo, F. Colloidal Self-assembled Nanosphere Arrays for Plasmon-enhanced Light Trapping in Thin Film Silicon Solar Cells. *Energy Procedia* **2014**, *44*, 184-191.

15. Dudek, M.; Zajac, G.; Szafraniec, E.; Wiercigroch, E.; Tott, S.; Malek, K.; Kaczor, A.; Baranska, M. Raman Optical Activity and Raman spectroscopy of carbohydrates in solution. *Spectrochimica Acta Part A: Molecular and Biomolecular Spectroscopy* **2019**, *206*, 597-612.

16. Garcia, M. A. *J. Phys. D: Appl. Phys*. **2011**, 44, 283001

17. Zhang, Q.; Wang, X. -D.; Tian, T.; Chu, L. -Q. Incorporation of multilayered silver nanoparticles into polymer brushes as 3-dimensional SERS substrates and their application for bacteria detection. *Appl. Surf. Sci.* **2017**, 407, 185-191.

18. Aminfard, S.; Harrison, R. K.; Ben-Yakar, A. Enhanced optical absorption in ultrathin silicon films using embedded silica-coated silver nanoparticles. *Optics Communications* **2019**, *430*, 143-150.

19. Zhang, X.; Young, M. A.; Lyandres, O.; Van Duyne, R. P. Rapid Detection of an Anthrax Biomarker by Surface-Enhanced Raman Spectroscopy. *J. Am. Chem. Soc.* **2005**, *127*, 4484-4489.

20. Chou, S.; Yu, C.; Yen, Y.; Lin, K.; Chen, H.; Su, W. Romantic Story or Raman Scattering? Rose Petals as Ecofriendly, Low-Cost Substrates for Ultrasensitive Surface-Enhanced Raman Scattering. *Anal. Chem.* **2015**, *87*, 6017-6024.

21.Yuan, K.; Zheng, J.; Yang, D.; Jurado SÃ¡nchez, B.; Liu, X.; Guo, X.; Liu, C.; Dina, N. E.; Jian, J.; Bao, Z.; Hu, Z.; Liang, Z.; Zhou, H.; Jiang, Z. Self-Assembly of Au@Ag Nanoparticles on Mussel Shell To Form Large-Scale 3D Supercrystals as Natural SERS Substrates for the Detection of Pathogenic Bacteria. *ACS Omega* **2018**, *3*, 2855-2864.

22. Li, Y.; Ye, Y.; Fan, Y.; Zhou, J.; Jia, L.; Tang, B.; Wang, X. Silver Nanoprism-Loaded Eggshell Membrane: A Facile Platform for In Situ SERS Monitoring of Catalytic Reactions. *Crystals* **2017**, *7*, 45.

23. Li, R.; Shi, G.; Wang, Y.; Wang, M.; Zhu, Y.; Sun, X.; Xu, H.; Chang, C. Decoration of Cu films on the microstructural mantis wing as flexible substrates for surface enhanced Raman scattering. *Optik* **2018**, *172*, 49-56.

24. Syu, W.; Lin, Y.; Paliwal, A.; Wang, K.; Liu, T. Highly sensitive and reproducible SERS substrates of bilayer Au and Ag nano-island arrays by thermal evaporation deposition. *Surface and Coatings Technology* **2018**, *350*, 823-830.

25. Radloff, C.; Vaia, R.; Brunton, J.; Bouwer, G.; Ward, V. Metal nanoshell assembly on a virus bioscaffold. *Nano Letters* **2005**, *5*, 1187-1191.

26. Stiles, P. L.; Dieringer, J. A.; Shah, N. C.; Van Duyne, R. P. Surface-Enhanced Raman Spectroscopy. *Annual Rev. Anal. Chem.* **2008**, *1*, 601-626.

27. Parker, A. R.; Martini, N. Structural colour in animals—simple to complex optics. *Optics & Laser Technology* **2006**, *38*, 315-322.

28. Malhotra, B. D.; Ali, M. A. Chapter 7 - Nanostructured Biomaterials for In Vivo Biosensors. **2018**, 183-219.

29. Cai, H.; Wu, Y.; Dai, Y.; Pan, N.; Tian, Y.; Luo, Y.; Wang, X. Wafer scale fabrication of highly dense and uniform array of sub-5 nm nanogaps for surface enhanced Raman scatting substrates. *Optics Express* **2016**, *24*, 20808-20815.

30. Schlegel, V. L.; Cotton, T. M. Silver-island films as substrates for enhanced Raman scattering: effect of deposition rate on intensity. *Anal. Chem.* **1991**, *63*, 241-247.

31. van Duyne, R.,P.; Hulteen, J.,C.; Treichel, D.,A. *Atomic force microscopy and surface-enhanced Raman spectroscopy. I. Ag island films and Ag film over polymer nanosphere surfaces supported on glass;* 1993; Vol. 99, pp 2101-2115.

32. Kosuda, K. M.; Bingham, J. M.; Wustholz, K. L.; Van Duyne, R. P. 3.09 - Nanostructures and Surface-Enhanced Raman Spectroscopy. **2011**, 263-301.

33. Mao, Y.; Ai, H.; Chen, Y.; Zhang, Z.; Zeng, P.; Kang, L.; Li, W.; Gu, W.; He, Q.; Li, H. Phytoplankton response to polystyrene microplastics: Perspective from an entire growth period. *Chemosphere* **2018**, *208*, 59-68.

34. Bumbrah, G. S.; Sharma, R. M. Raman spectroscopy – Basic principle, instrumentation and selected applications for the characterization of drugs and abuse. *Egypt. J. Forensic Sci.* **2016**, 6, 209-215.

35. Elshorbagy, M. H.; Cuadrado, A.; Alda, J. Plasmonic Sensor Based on Dielectric Nanoprisms. *Nanoscale Research Letters* **2017**, *12*, 580.

36. Mansour, H. M.; Hickey, A. J. Raman characterization and chemical imaging of biocolloidal self- assemblies, drug delivery systems, and pulmonary inhalation aerosols: A review. *Aaps Pharmscitech* **2007**, *8*, 99.

37. Ferraro, J. R.; Nakamoto, K. In *Basic Theory;* Introductory Raman Spectroscopy; Academic Press: 1250 Sixth Avenue, San Diego, CA, **1994**, 1-90.

38. Pan, N.; Sun, G. *Functional textiles for improved performance, protection and health;* Elsevier: **2011**, 26-40.

39. Thornton, J. A. Influence of substrate temperature and deposition rate on structure of thick sputtered Cu coatings. *Journal of Vacuum Science and Technology* **1975**, *12*, 830-835.

40. Wang, M.; Wang, Y.; Yan, X.; Sun, X.; Shi, G.; Zhang, K.; Ren, L.; Ma, W. Three-Dimensional Hierarchical Reticular Nanostructure of *Fulfora candelaria* Wing Decorated by Ag Nanoislands as Practical SERS-Active Substrates. *Nanomaterials* **2018**, *8*, 905.

41. Kobayashi, F.; Nomura, A.; Kano, T. Effects of deposition rate control process on the adhesion of evaporated aluminum films. *Electronics and Communications in Japan (Part II: Electronics)* **1996**, *79*, 76-85.

42, Dong, W.; Zhang, T.; Epstein, J.; Cooney, L.; Wang, H.; Li, Y.; Jiang, Y.; Cogbill, A.; Varadan, V.; Tian, Z. R. Multifunctional nanowire bioscaffolds on titanium. Chemistry of Materials **2007**, 19, 4454-4459.

43. Grant, S. A.; Spradling, C. S.; Grant, D. N.; Fox, D. B.; Jimenez, L.; Grant, D. A.; Rone, R. J. Assessment of the biocompatibility and stability of a gold nanoparticle collagen bioscaffold. *Journal of Biomedical Materials Research Part a* **2014**, *102*, 332-339.

44. Kreno, L. E.; Greeneltch, N. G.; Farha, O. K.; Hupp, J. T.; Van Duyne, R. P. SERS of molecules that do not adsorb on Ag surfaces: a metal organic framework-based functionalization strategy. *Analyst* **2014**, *139*, 4073-4080.

45. Mikac, L.; Ivanda, M.; Gotić, M.; Janicki, V.; Zorc, H.; Jančі, T.; Vidaček, S. Surface-enhanced Raman spectroscopy substrate based on Ag-coated self-assembled polystyrene spheres. *Journal of Molecular Structure* **2017**, *1146*, 530-535.

46. Stoddart, P.; Cadusch, P.; Boyce, T.; Erasmus, R.; Comins, J. Optical properties of chitin: surface-enhanced Raman scattering substrates based on antireflection structures on cicada wings. *Nanotechnology* **2006**, *17*, 680-686.

47. Hwang, H.; Kim, S.; Yang, S. Microfluidic fabrication of SERS-active microspheres for molecular detection. Lab on a Chip 2011, 11, 87-92.

48. Cai, W. B.; Ren, B.; Li, X. Q.; She, C. X.; Liu, F. M.; Cai, X. W.; Tian, Z. Q. *Surf. Sci.***1998**, *406*, 9-22.

49. Lee, C. H.; Hankus, M. E.; Tian, L.; Pellegrino, P. M.; Singamaneni, S. Highly sensitive surface enhanced Raman scattering substrates based on filter paper loaded with plasmonic nanostructures. *Anal. Chem.* **2011**, *83*, 8953-8958.

50. Aroca, R. Surface-Enhanced Vibrational Spectroscopy. University of Windsor, Ontario, Canada, **2006.**

51. Lv, M. Y.; Teng, H. Y.; Chen, Z. Y.; Zhao, Y. M.; Zhang, X.; Liu, L.; Wu, Z.; Liu, L. M.; Xu, H. J. Low-cost Au nanoparticle-decorated cicada wing as sensitive and recyclable substrates for surface enhanced Raman scattering. *Sensors and Actuators B: Chemical* **2015**, *209*, 820-827.

52. Rubira, R. J. G.; Camacho, S. A.; Aoki, P. H. B.; Maximino, M. D.; Alessio, P.; Martin, C. S.; Oliveira, O. N., Jr.; Fatore, F. M.; Paulovich, F. V.; Constantino, C. J. L.

Detection of trace levels of atrazine using surface-enhanced Raman scattering and information visualization. *Colloid Polym. Sci.* **2014**, *292*, 2811-2820.

Appendix

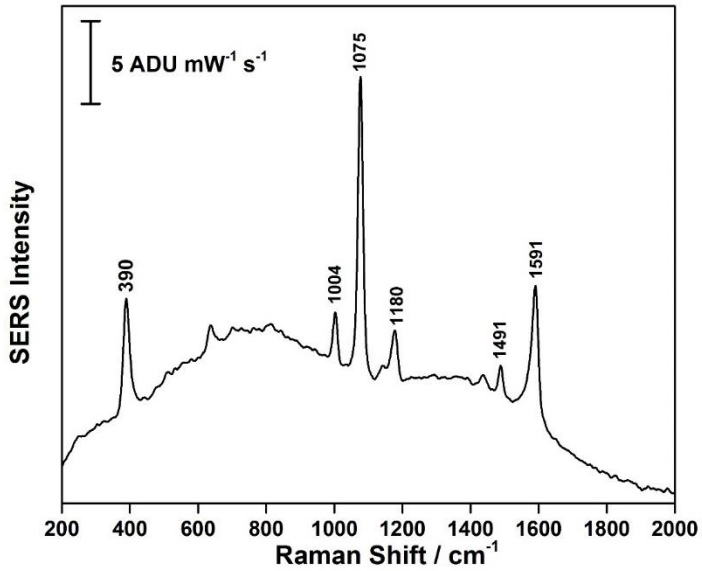

A1: Average SERS spectra of p-ATP drop-coated on beetle elytra- 50 nm Ag deposition. (780 nm laser, 12.17 mW and acquisition time of 30 seconds)

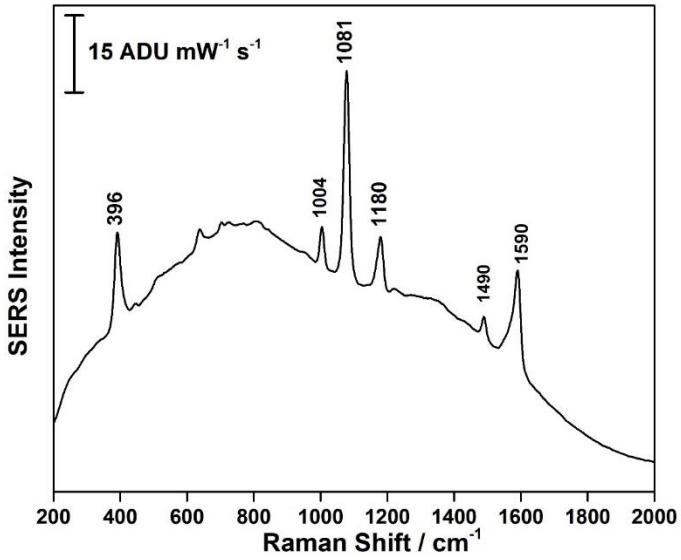

A2: Average SERS spectra of p-ATP drop-coated on beetle elytra- 100 nm Ag deposition. (780 nm laser, 12.17 mW and acquisition time of 30 seconds)

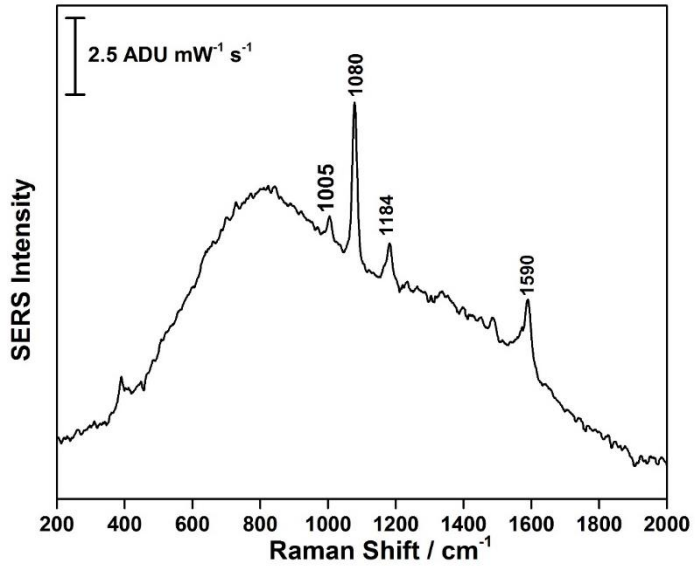

A3: Average SERS spectra of p-ATP drop-coated on beetle elytra- 150 nm Ag deposition. (780 nm laser, 12.17 mW and acquisition time of 30 seconds)

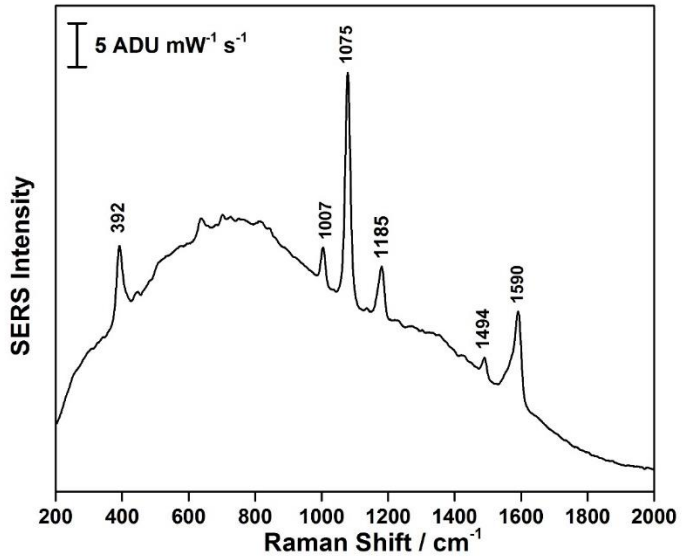

A4: Average SERS spectra of p-ATP drop-coated on beetle elytra- 200 nm Ag deposition. (780 nm laser, 12.17 mW and acquisition time of 30 seconds)

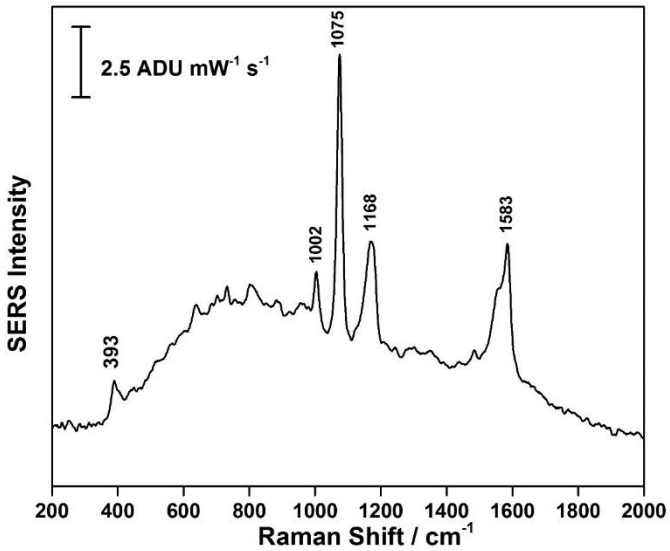

A5: Average SERS spectra of p-ATP drop-coated on buttercup petal- 50 nm Ag deposition. (780 nm laser, 12.17 mW and acquisition time of 30 seconds)

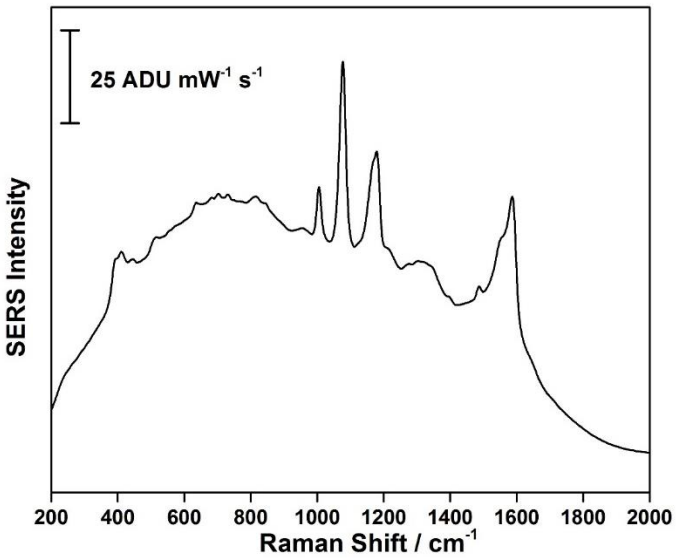

A6: Average SERS spectra of p-ATP drop-coated on buttercup petal- 100 nm Ag deposition. (780 nm laser, 12.17 mW and acquisition time of 30 seconds)

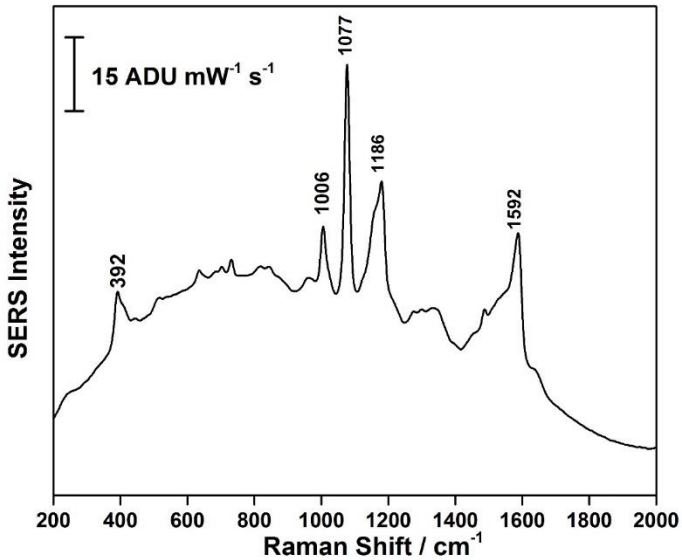

A7: Average SERS spectra of p-ATP drop-coated on buttercup petal- 150 nm Ag deposition. (780 nm laser, 12.17 mW and acquisition time of 30 seconds)

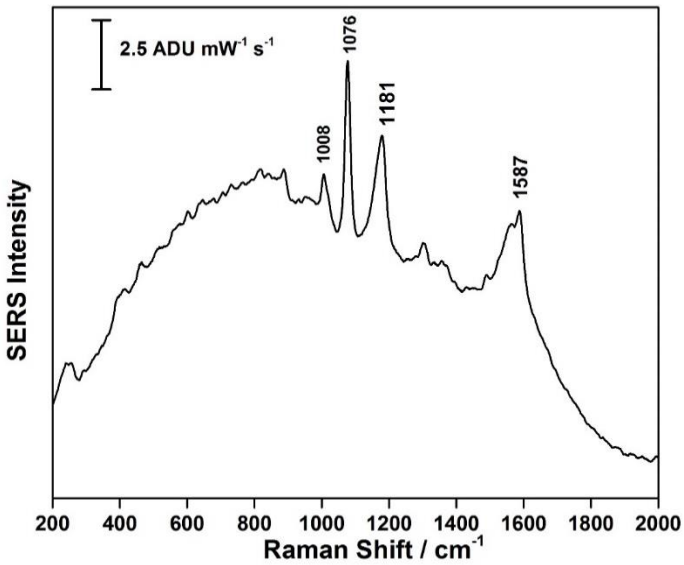

A8: Average SERS spectra of p-ATP drop-coated on buttercup petal- 200 nm Ag deposition. (780 nm laser, 12.17 mW and acquisition time of 30 seconds)

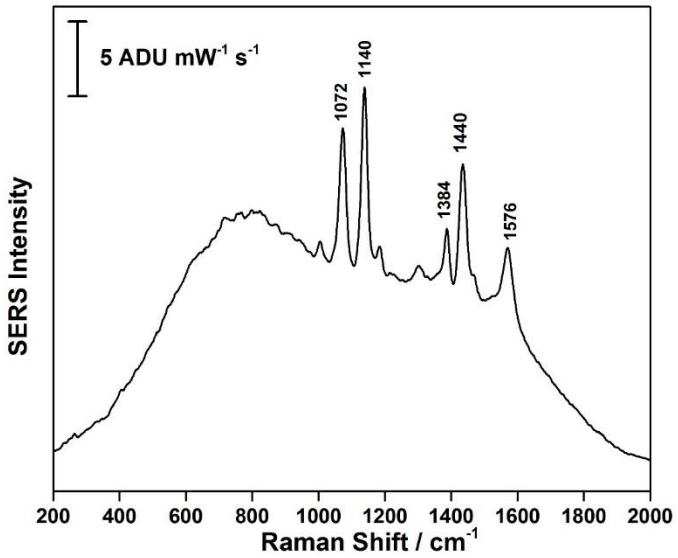

A9: Average SERS spectra of p-ATP drop-coated on damselfly wing- 50 nm Ag deposition. (780 nm laser, 12.17 mW and acquisition time of 30 seconds)

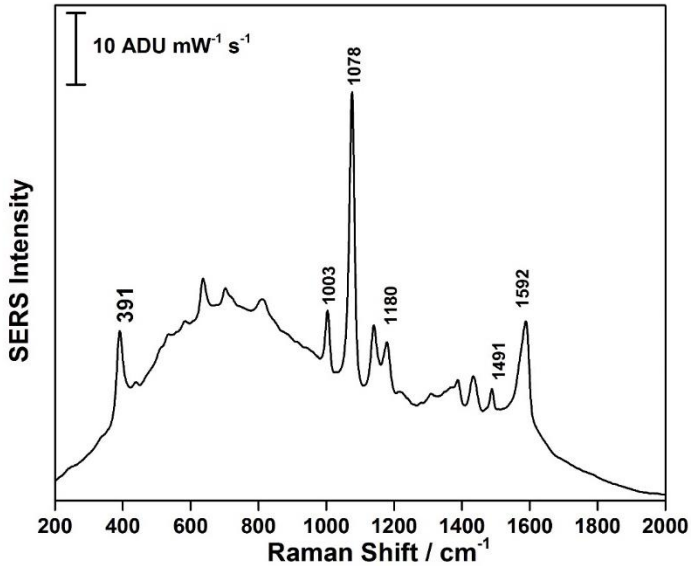

A10: Average SERS spectra of p-ATP drop-coated on damselfly wing- 100 nm Ag deposition. (780 nm laser, 12.17 mW and acquisition time of 30 seconds)

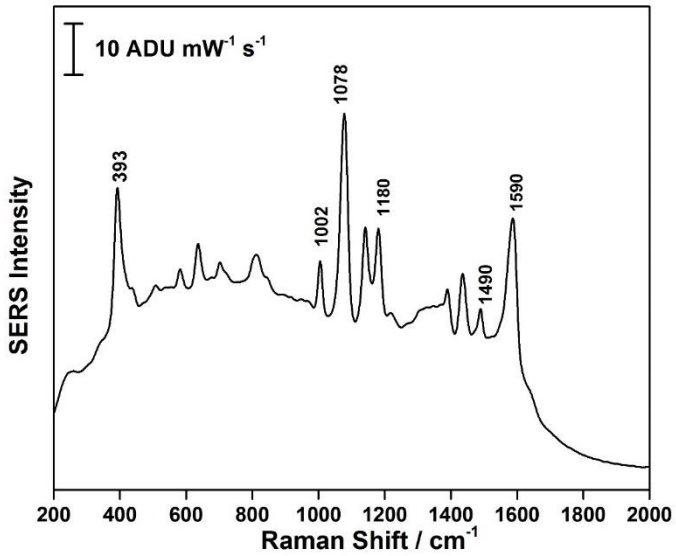

A11: Average SERS spectra of p-ATP drop-coated on damselfly wing- 150 nm Ag deposition. (780 nm laser, 12.17 mW and acquisition time of 30 seconds)

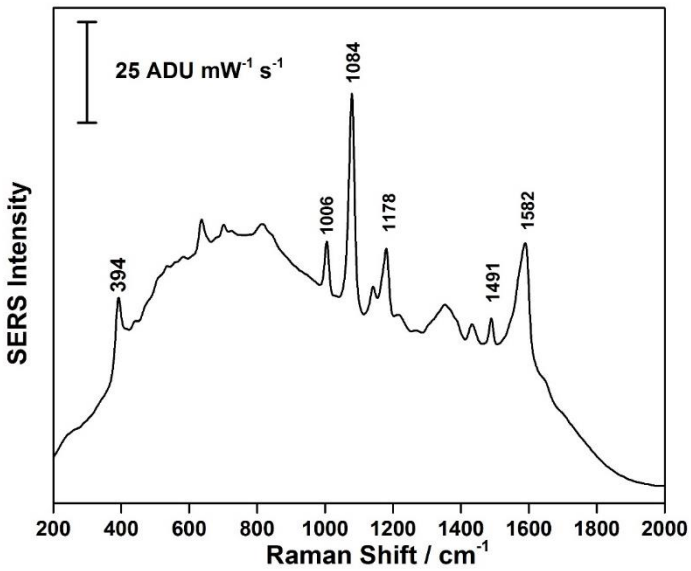

A12: Average SERS spectra of p-ATP drop-coated on damselfly wing- 200 nm Ag deposition. (780 nm laser, 12.17 mW and acquisition time of 30 seconds)

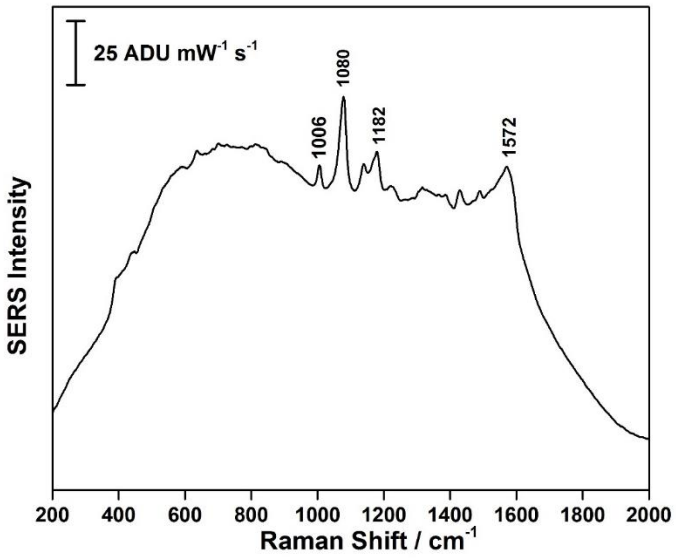

A13: Average SERS spectra of p-ATP on damselfly wing- 50 rpm (780 nm laser, 12.17 mW and acquisition time of 30 seconds).

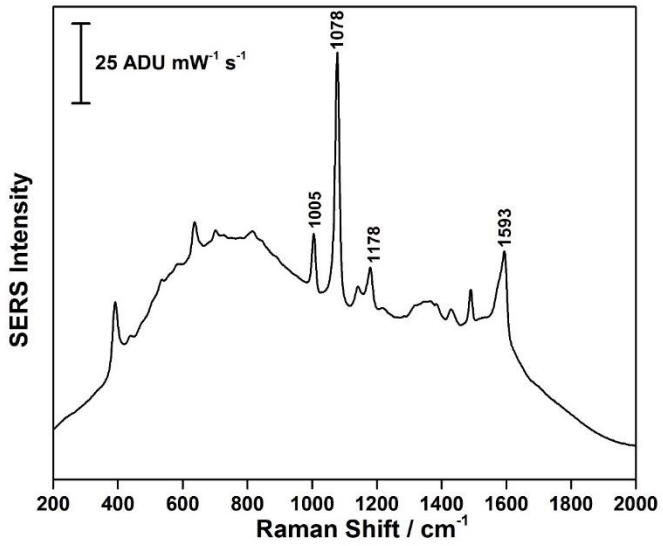

A14: Average SERS spectra of p-ATP on damselfly wing- 80 rpm (780 nm laser, 12.17 mW and acquisition time of 30 seconds).

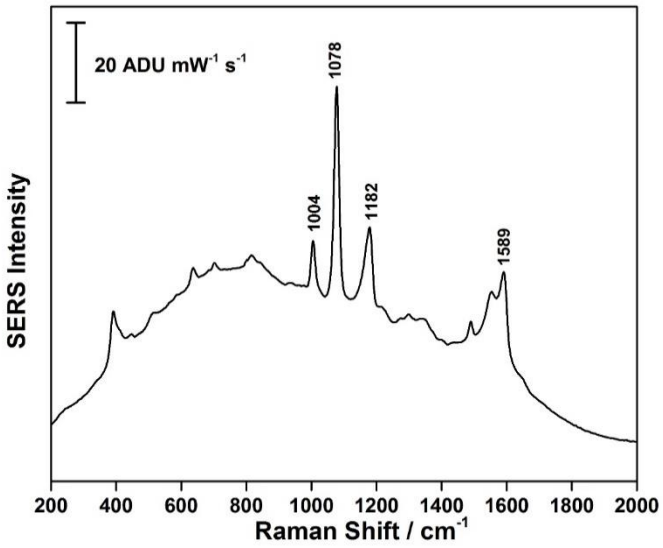

A15: Average SERS spectra of p-ATP on buttercup petal- 80 rpm (780 nm laser, 12.17 mW and acquisition time of 30 seconds).

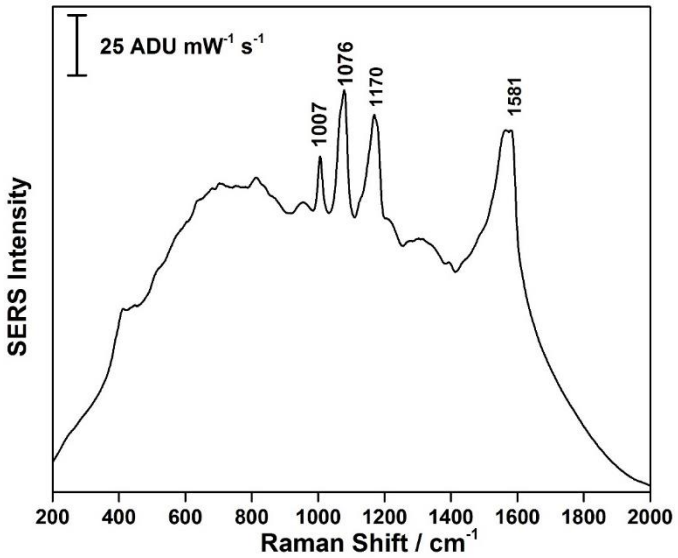

A16: Average SERS spectra of p-ATP on buttercup petal- 1.00 Å/s (780 nm laser, 12.17 mW and acquisition time of 30 seconds).

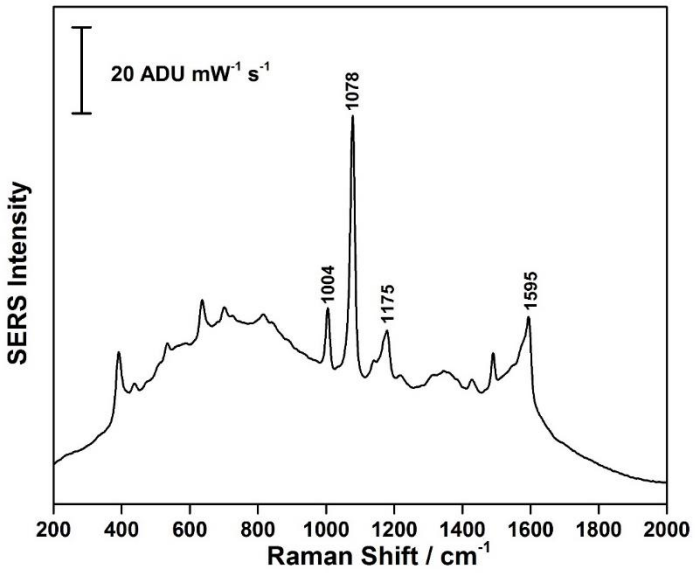

A17: Average SERS spectra of p-ATP on damselfly wing- 4.00 Å/s (780 nm laser, 12.17 mW and acquisition time of 30 seconds).

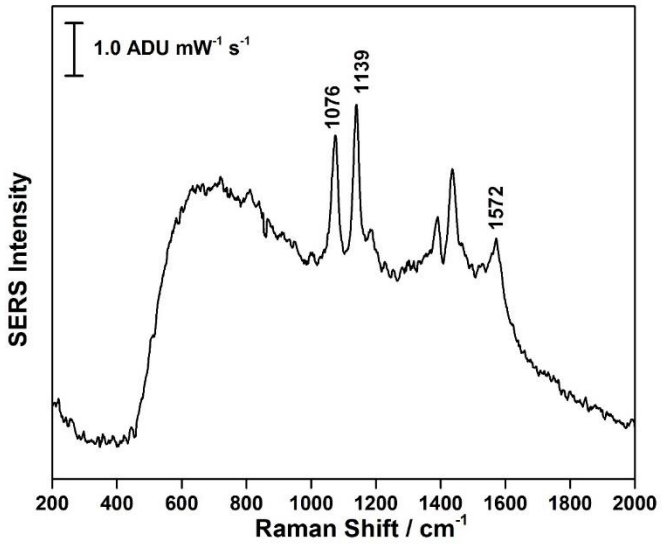

A18: Average SERS spectra of p-ATP on damselfly wing- 2.5 A (780 nm laser, 12.17 mW and acquisition time of 30 seconds).

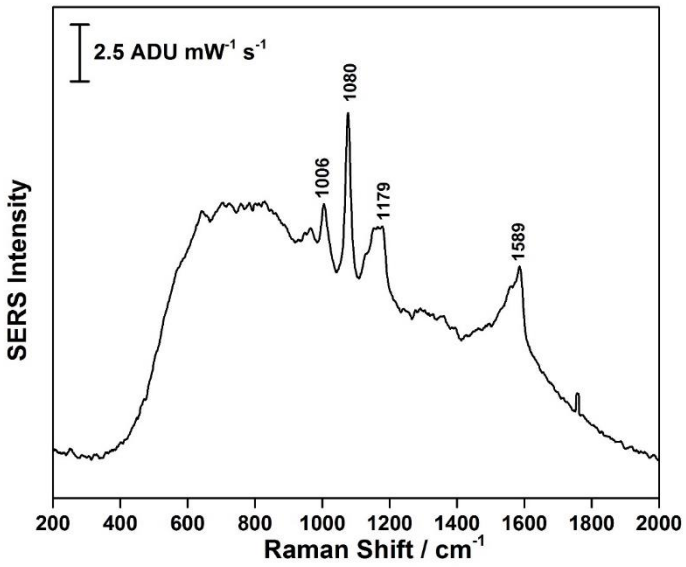

A19: Average SERS spectra of p-ATP on buttercup petal- 2.5 A (780 nm laser, 12.17 mW and acquisition time of 30 seconds).

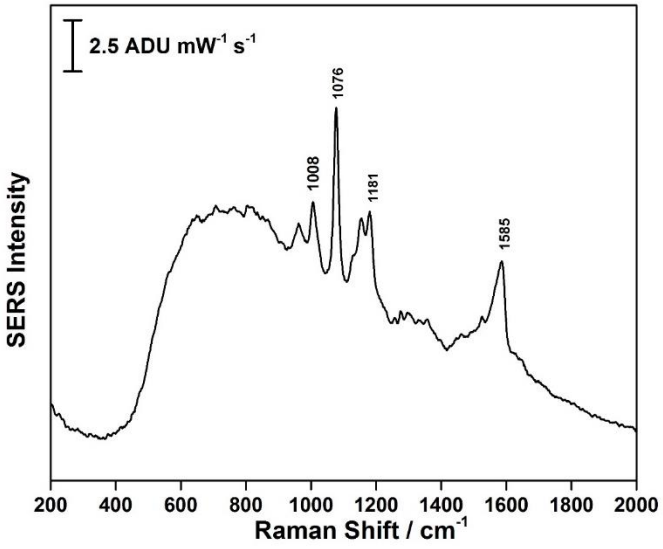

A20: Average SERS spectra of p-ATP on buttercup petal- 10 A (780 nm laser, 12.17 mW and acquisition time of 30 seconds).

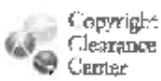

RightsLink

Home | Create Account | Help

Title:	Controlling the Synthesis and Assembly of Silver Nanostructures for Plasmonic Applications
Author:	Matthew Rycenga, Claire M. Cobley, Zhe Zeng, et al
Publication:	Chemical Reviews
Publisher:	American Chemical Society
Date:	Jun 1, 2011

PERMISSION/LICENSE IS GRANTED FOR YOUR ORDER AT NO CHARGE

This type of permission/license, instead of the standard Terms & Conditions, is sent to you because no fee is being charged for your order. Please note the following:

- Permission is granted for your request in both print and electronic formats, and translations.
- If figures and/or tables were requested, they may be adapted or used in part.
- Please print this page for your records and send a copy of it to your publisher/graduate school.
- Appropriate credit for the requested material should be given as follows: "Reprinted (adapted) with permission from (COMPLETE REFERENCE CITATION). Copyright (YEAR) American Chemical Society." Insert appropriate information in place of the capitalized words.
- One-time permission is granted only for the use specified in your request. No additional uses are granted (such as derivative works or other editions). For any other uses, please submit a new request.

If credit is given to another source for the material you requested, permission must be obtained from that source.

BACK | CLOSE WINDOW